

## COBE-DMR-Normalized Dark Energy Cosmogony

Pia Mukherjee<sup>1,2</sup>, A. J. Banday<sup>3</sup>, Alain Riazuelo<sup>4</sup>, Krzysztof M. Górski<sup>5,6</sup>, and Bharat Ratra<sup>1</sup>

### ABSTRACT

Likelihood analyses of the COBE-DMR sky maps are used to determine the normalization of the inverse-power-law-potential scalar field dark energy model. Predictions of the DMR-normalized model are compared to various observations to constrain the allowed range of model parameters. Although the derived constraints are restrictive, evolving dark energy density scalar field models remain an observationally-viable alternative to the constant cosmological constant model.

*Subject headings:* cosmic microwave background — cosmology: observation — large-scale structure of the universe

### 1. Introduction

Indications are that at the present epoch the universe is dominated by dark energy (see, e.g., Peebles & Ratra 2003 for a review and Bennett et al. 2003a for a summary of the recent WMAP results). Einstein’s cosmological constant  $\Lambda$  is the earliest example of dark energy, and more recently scalar field models in which the energy density slowly decreases with time, and thus behaves like a time-variable  $\Lambda$ , have been the subject of much study (see, e.g., Peebles 1984; Peebles & Ratra 1988, 2003; Padmanabhan 2003).<sup>7</sup>

In this paper we focus on a simple dark energy scalar field ( $\phi$ ) model. In this model the scalar field potential energy density  $V(\phi)$  at low redshift is  $\propto \phi^{-\alpha}$ , with  $\alpha > 0$  (see, e.g., Peebles & Ratra 1988; Ratra & Peebles 1988). Consistent with the observational indications, the cosmological model is taken to be spatially flat (see, e.g., Podariu et al. 2001b; Durrer, Novosyadlyj, & Apuneyvych 2003; Page et al. 2003; Melchiorri & Ödman 2003).

---

<sup>1</sup>Department of Physics, Kansas State University, 116 Cardwell Hall, Manhattan, KS 66506.

<sup>2</sup>Present address: Department of Physics and Astronomy, University of Oklahoma, 440 W. Brooks Street, Norman, OK 73019.

<sup>3</sup>Max-Planck Institut für Astrophysik, Karl-Schwarzschildstrasse 1, Garching D-85741, Germany.

<sup>4</sup>Service de Physique Théorique, CEA/DSM/SPhT, Unité de recherche associée au CNRS, CEA/Saclay F-91191 Gif-sur-Yvette cédex, France.

<sup>5</sup>Jet Propulsion Laboratory, California Institute of Technology, MS 169-327, 4800 Oak Grove Drive, Pasadena, CA 91109.

<sup>6</sup>Warsaw University Observatory, Aleje Ujazdowskie 4, 00-478 Warszawa, Poland.

<sup>7</sup>Recent discussions of dark energy models include Dvali & Turner (2003), Wetterich (2003), Carroll, Hoffman, & Trodden (2003), Saini, Padmanabhan, & Bridle (2003), Jain, Dev, & Alcaniz (2003), Rosati (2003), Alam, Sahni, & Starobinsky (2003), Munshi, Porciani, & Wang (2003), Caldwell, Kamionkowski, & Weinberg (2003), Klypin et al. (2003), Silva & Bertolami (2003), Sen & Sen (2003), and Singh, Sami, & Dadhich (2003), through which the earlier literature may be accessed.

Dark energy models, which assume an early epoch of inflation to generate the needed initial energy density fluctuations, do not predict the amplitude of these fluctuations. At present, the most robust method to fix this amplitude, and hence the normalization of the model, is to compare model predictions of the large angular scale spatial anisotropy in the cosmic microwave background (CMB) radiation to what is observed. To this end we compute the model predictions as a function of the parameter  $\alpha$  and other cosmological parameters by following Brax, Martin, & Riazuelo (2000). We then determine the normalization amplitude by comparing these predictions to the COBE-DMR CMB anisotropy measurements (Bennett et al. 1996) by following Górski et al. (1998).

In linear perturbation theory, a scalar field is mathematically equivalent to a fluid with time-dependent equation of state parameter  $w = p/\rho$  and speed of sound squared  $c_s^2 = \dot{p}/\dot{\rho}$ , where  $p$  is the pressure,  $\rho$  the energy density, and the dots denote time derivatives (see, e.g., Ratra 1991). The XCDM parametrization of this dark energy model approximates  $w$  as a constant, which is accurate in the radiation and matter dominated epochs but not in the current, dark energy scalar field dominated epoch. This XCDM approximation leads to particularly inaccurate predictions for the large angular scale CMB anisotropy. We emphasize, however, that we do not work in the XCDM approximation, rather we explicitly integrate the dark energy scalar field and other equations of motion (Brax et al. 2000).

With a robust determination of the normalization of the inverse-power-law potential dark energy scalar field it is possible to test the model and constrain model parameter values by comparing other model predictions to observational data. In this paper we compare the predicted value, as a function of model parameters, of the rms linear mass fluctuation averaged over an  $8 h^{-1}$  Mpc sphere<sup>8</sup>,  $\delta M/M(8h^{-1}\text{Mpc})$  or  $\sigma_8$ , to observational estimates of this quantity. We also present qualitative comparisons of the predicted fractional energy-density perturbation power spectrum  $P(k)$  to various observations.

Such tests probe a combination of both the early universe physics of inflation and late universe dark energy physics. Other neoclassical cosmological tests are largely insensitive to the early universe physics of inflation and are hence more direct probes of dark energy. Of special interest are tests based on gravitational lensing (see, e.g., Ratra & Quillen 1992; Waga & Frieman 2000; Chae et al. 2002), Type Ia supernovae redshift-apparent magnitude (see, e.g., Podariu & Ratra 2000; Waga & Frieman 2000; Leibundgut 2002; Tonry et al. 2003), and redshift-angular size (see, e.g., Chen & Ratra 2003a; Podariu et al. 2003; Zhu & Fujimoto 2003, also see Daly & Djorgovski 2003) data.

In § 2 we summarize the techniques we use to determine the DMR estimate of the CMB rms quadrupole moment anisotropy amplitude  $Q_{\text{rms-PS}}$  for the inverse-power-law potential dark energy scalar field model. Results for  $Q_{\text{rms-PS}}$  and large-scale structure statistics for the DMR-normalized models are given in § 3. These statistics are compared to current observational measurements in § 4. Our results are summarized in § 5.

## 2. Summary of Computation

We consider a scale-invariant primordial energy-density fluctuation power spectrum (Harrison 1970; Peebles & Yu 1970; Zel'dovich 1972), as is generated by quantum fluctuations in a weakly coupled scalar field during an early epoch of inflation (see, e.g., Fischler, Ratra, & Susskind 1985), and consistent with

---

<sup>8</sup>Here the Hubble constant  $H_0 = 100h \text{ km s}^{-1} \text{ Mpc}^{-1}$ .

the observational indications (see, e.g., Spergel et al. 2003). More precisely, the fractional energy-density perturbation power spectrum we consider is

$$P(k) = A k T^2(k), \quad (1)$$

where  $k$  ( $0 < k < \infty$ ) is the magnitude of the coordinate spatial wavenumber,  $T(k)$  is the transfer function, and  $A$  is the normalization amplitude defined in terms of the Bardeen potential.

The CMB fractional temperature perturbation,  $\delta T/T$ , is expressed as a function of angular position,  $(\theta, \phi)$ , on the sky via the spherical harmonic decomposition,

$$\frac{\delta T}{T}(\theta, \phi) = \sum_{\ell=2}^{\infty} \sum_{m=-\ell}^{\ell} a_{\ell m} Y_{\ell m}(\theta, \phi). \quad (2)$$

The CMB spatial anisotropy in a Gaussian model<sup>9</sup> can then be characterized by the angular perturbation spectrum  $C_{\ell}$ , defined in terms of the ensemble average,

$$\langle a_{\ell m} a_{\ell' m'}^* \rangle = C_{\ell} \delta_{\ell \ell'} \delta_{mm'}, \quad (3)$$

where the  $\delta$ 's are Kronecker delta functions.

The  $C_{\ell}$ 's used here were computed using the Boltzmann transfer code of Brax et al. (2000). The computations here assume a standard recombination thermal history, and ignore the possibility of early reionization, tilt, gravity waves, or space curvature. While observed early reionization (Bennett et al. 2003a) does affect the  $C_{\ell}$ 's on the large angular scales of interest here, the effect is not large and an accurate quantitative estimate awaits a better understanding of structure formation. At present there is not much observational motivation for the inclusion of tilt, gravity waves, or space curvature.

The dark energy scalar field model we consider here is characterized by the potential energy density function

$$V(\phi) = \kappa \phi^{-\alpha}, \quad (4)$$

where the constant  $\kappa$  has dimensions of mass raised to the power  $\alpha + 4$  (Peebles & Ratra 1988). In the limit where the exponent  $\alpha$  approaches zero, the scalar field energy density is equivalent to a constant cosmological constant  $\Lambda$ . Here the exponent  $\alpha \geq 0$ .

We evaluate the CMB anisotropy angular spectra for a range of inverse-power-law scalar field potential exponent  $\alpha$  spanning the interval between 0 and 8 in steps of unity, a range of  $\Omega_0$  spanning the interval between 0.1 and 1 in steps of 0.1 and for  $\Omega_0 = 0.05$ , and for a variety of values of  $h$  and the baryonic-mass density parameter  $\Omega_B$ . The values of  $h$  were selected to cover the range of ages consistent with current requirements ( $t_0 = 11$  Gyr, 13 Gyr, or 17 Gyr, see, e.g., Peebles & Ratra 2003), with  $h$  as a function of  $\Omega_0$  computed accordingly. The values of  $\Omega_B$  were chosen to be consistent with current standard nucleosynthesis constraints ( $\Omega_B h^2 = 0.006, 0.014$ , or  $0.022$ , see, e.g., Peebles & Ratra 2003). To render the problem tractable,  $C_{\ell}$ 's were determined for the central values of  $t_0$  and  $\Omega_B h^2$ , and for the two combinations of these parameters which most perturb the  $C_{\ell}$ 's from those computed at the central values (i.e., for the smallest  $t_0$  we used the smallest  $\Omega_B h^2$ , and for the largest  $t_0$  we used the largest  $\Omega_B h^2$ ). Specific parameter values are given in

---

<sup>9</sup>Simple inflation models are Gaussian, with fluctuations generated in a weakly coupled field (see, e.g., Ratra 1985; Fischler et al. 1985), consistent with observational indications (see, e.g., Mukherjee, Hobson, & Lasenby 2000; Park et al. 2001; Komatsu et al. 2002, 2003; Santos et al. 2002; De Troia et al. 2003).

columns (1) and (2) of Tables 1–3, and representative CMB anisotropy power spectra can be seen in Figs. 1 and 2.

The differences in the low- $\ell$  shapes of the  $C_\ell$ 's in Figs. 1 and 2 are a consequence of the interplay between the “usual” (fiducial CDM) Sachs-Wolfe term and the “integrated” Sachs-Wolfe term in the expression for the CMB spatial anisotropy (see, e.g., Hu & Dodelson 2002 for a review). The relative importance of these terms is determined by the values of  $\Omega_0$  and  $\alpha$ . (These terms are not easy to estimate analytically, and we can not trust the inaccurate XCDM approximation and must instead rely on numerical computations because these terms depend in complicated ways on the way in which  $w$  changes from its value during the matter dominated epoch to its value at zero redshift.) More precisely, in dark energy models the gravitational potential decays with time at late time, so at late time the gravitational potential and its time derivative are of opposite sign. Consequently there is some anticorrelation between the usual and integrated Sachs-Wolfe terms. This anticorrelation more significantly reduces the  $C_\ell$ 's at larger  $\Omega_0$  (where the integrated term is not too large) and larger  $\alpha$  (because the transition from matter dominance to dark energy dominance occurs earlier).

The normalization of the theoretical CMB anisotropy spectra are determined by comparing them to the DMR data using the likelihood analysis method of Górski (1994). In this paper we utilize the DMR four-year co-added 53 and 90 GHz sky maps in galactic coordinates. We do not consider the DMR ecliptic coordinates data here; the small shifts in the inferred normalization amplitudes due to the small differences in the galactic- and ecliptic-coordinate maps are quantified in Górski et al. (1998). The 53 and 90 GHz maps are coadded using inverse-noise-variance weights. The main changes relative to the analysis of Gorski et al. (1998) are that we use the DMR maps in the HEALPix pixelisation, and excise pixels likely to be contaminated by bright foreground emission on and near the Galactic plane (Banday et al. 1997) using a cut rederived from the DIRBE 140  $\mu\text{m}$  data. The DIRBE map was reconstructed in the HEALPix format using the publicly available Calibrated Individual Observations (CIO) files together with the DIRBE Sky and Zodi Atlas (DSZA, both products being described in Hauser et al. 1998), allowing the construction of a full sky map corrected for the zodiacal emission according to the model of Kelsall et al. (1998). We consider  $C_\ell$ 's to multipole  $\ell \leq 30$ . See Górski et al. (1998) for a more detailed description of the method.

As mentioned, we excise sky-map pixels on and near the Galactic plane where foreground emission dominates the CMB. Following Górski et al. (1998, also see Górski et al. 1995, 1996) we quantify the extent to which residual high-latitude Galactic emission can modify our results in two ways: by performing all computations both including and excluding the observed sky quadrupole, and by performing all computations with and without correcting for emission correlated with the DIRBE 140  $\mu\text{m}$  sky map, itself fitted to the data for each model.<sup>10</sup>

### 3. Results

#### 3.1. Results of $Q_{\text{rms-PS}}$ fitting

The results of the DMR likelihood analysis are summarized in Figs. 3–9 and Tables 1–3.

We have computed DMR data likelihood functions  $L(Q_{\text{rms-PS}}, \Omega_0, \alpha)$  using three sets of  $C_\ell$ 's computed

---

<sup>10</sup>See Górski et al. (1998) for a more detailed discussion. More recent discussions of foreground emissions may be accessed through Mukherjee et al. (2002, 2003b), Banday et al. (2003), and Bennett et al. (2003b).

for values of  $(\Omega_B h^2, t_0) = (0.014, 13 \text{ Gyr})$ ,  $(0.006, 11 \text{ Gyr})$ , and  $(0.022, 17 \text{ Gyr})$ . We have also considered four “different” DMR data sets, either accounting for or ignoring the correction for faint high-latitude foreground Galactic emission, and either including or excluding the quadrupole moment from the analysis.

Variations in  $\Omega_0$  and  $\alpha$  have the largest effect on the inferred value of  $Q_{\text{rms-PS}}$  from the DMR data. Changes in  $\Omega_B h^2$ ,  $t_0$ , faint high-latitude Galactic emission treatment, and quadrupole moment treatment, have much smaller effects, consistent with the findings of Górski et al. (1998). These results determine what we have chosen to display in Figs. 3–9 and Tables 1–3.

Two representative sets of likelihood functions  $L(Q_{\text{rms-PS}}, \Omega_0)$  are shown in Figs. 3 and 4. Figure 3 shows those derived while accounting for the correction for faint high-latitude foreground Galactic emission, and including the quadrupole moment in the analysis. Figure 4 shows the likelihood functions derived while ignoring the faint high-latitude foreground Galactic emission correction, and excluding the quadrupole moment from the analysis. These data sets represent two different ways of dealing with effects of foreground emission on the inferred  $Q_{\text{rms-PS}}$  normalization (with the former resulting in a typically 5 % lower  $Q_{\text{rms-PS}}$  value). These two data sets span the range of normalizations inferred from our analysis here.<sup>11</sup> The other two data sets we have used here, accounting for the faint high-latitude foreground emission while excluding the quadrupole and not accounting for the faint high-latitude foreground emission while including the quadrupole, result in  $Q_{\text{rms-PS}}$  normalizations that are typically 1–2 % above the smaller value or below the larger value of the first two data sets.

Tables 1–3 give the  $Q_{\text{rms-PS}}$  central values and 1 and 2  $\sigma$  ranges, computed from the appropriate posterior probability density distribution function assuming a uniform prior. These tables are computed for the three cases with  $\Omega_B h^2 = 0.014$  and  $t_0 = 13 \text{ Gyr}$  (Table 1),  $\Omega_B h^2 = 0.006$  and  $t_0 = 11 \text{ Gyr}$  (Table 2), and  $\Omega_B h^2 = 0.022$  and  $t_0 = 17 \text{ Gyr}$  (Table 3). We present results for four representative values of  $\alpha$  ( $= 0, 2, 4$ , and  $6$ ), and a range of values of  $\Omega_0$  spanning the interval from  $0.1$  to  $1$ .  $Q_{\text{rms-PS}}$  values are given only for the two extreme data sets whose likelihood functions are shown in Figs. 3 and 4: the faint high-latitude Galactic foreground emission corrected, quadrupole included case, and the Galactic foreground emission uncorrected quadrupole excluded case.

Figure 5 shows the ridge lines of maximum likelihood  $Q_{\text{rms-PS}}$  value, as a function of  $\Omega_0$ , for two different values of  $\alpha$ , for all four data sets used in this paper. The upper panels of Fig. 7 show the effect the small differences between data sets have on the conditional (fixed  $\Omega_0$ ,  $\alpha$ ,  $\Omega_B h^2$ , and  $t_0$ ) likelihood function for  $Q_{\text{rms-PS}}$ .

Tables 1–3 also illustrate the shift in the inferred  $Q_{\text{rms-PS}}$  normalization amplitudes due to changes in  $t_0$  and  $\Omega_B h^2$ . Figure 6 shows the effects that varying  $t_0$  and  $\Omega_B h^2$  have on the ridge lines of maximum likelihood  $Q_{\text{rms-PS}}$  as a function of  $\Omega_0$ . The lower panels of Fig. 7 show the effects varying  $t_0$  and  $\Omega_B h^2$  on the conditional (fixed  $\Omega_0$  and  $\alpha$ ) likelihood functions for  $Q_{\text{rms-PS}}$  for a given data set. On the whole, for the CMB anisotropy spectra considered here, shifts in  $t_0$  and  $\Omega_B h^2$  have only a small effect on the inferred normalization amplitude.

Future WMAP data (see, e.g., Bennett et al. 2003a) should be able to significantly constrain the dark energy scalar field model. Here we use the DMR normalized dark energy model predictions to semi-quantitatively constrain the cosmological parameters of this model. Since we do not attempt to determine precise constraints on these parameters in this paper, we do not combine results from analyses of all DMR

<sup>11</sup>The ecliptic-frame sky maps result in slightly larger inferred  $Q_{\text{rms-PS}}$  normalization values than the galactic-frame sky maps used here, see Górski et al. (1998).

data sets, as Górski et al. (1998) did for the open model (Gott 1982; Ratra & Peebles 1995), to determine the most robust estimate of the  $Q_{\text{rms-PS}}$  normalization amplitudes.

Figures 8 and 9 show marginal likelihood functions for some of the cosmological model parameter values and DMR data sets considered here. Figure 8 shows the likelihood function  $L(\Omega_0, \alpha)$  derived by marginalizing  $L(\Omega_0, \alpha, Q_{\text{rms-PS}})$  over  $Q_{\text{rms-PS}}$  with a uniform prior. Figure 9 shows conditional (on slices of constant  $\alpha$  or  $\Omega_0$ ) projections of the two-dimensional likelihood functions of Fig. 8. While the DMR data qualitatively indicate that lower  $\alpha$  and higher  $\Omega_0$  values are mildly favored, these data by themselves do not provide significant quantitative constraints on cosmological model parameter values.

### 3.2. Computation of Large-Scale Structure Statistics

The fractional energy-density perturbation power spectrum  $P(k)$  (eq. [1]) was evaluated from a numerical integration of the linear perturbation theory equations of motion. Table 4 lists the  $P(k)$  normalization amplitudes  $A$  (eq. [1]) for a range of  $\Omega_0$  and  $\alpha$  values.<sup>12</sup> The normalization amplitude is quite insensitive to the values of  $\Omega_B h^2$  and  $t_0$  used. It is more sensitive to the choice of DMR data set, and Fig. 10 shows representative  $P(k)$ ’s normalized to  $Q_{\text{rms-PS}}$  obtained by averaging those from the foreground-emission-corrected quadrupole-included analysis and the foreground-emission-uncorrected quadrupole-excluded analysis. Figure 10 also shows recent observational determinations of the galaxy power spectrum. The predicted matter power spectrum  $P(k) \propto (Q_{\text{rms-PS}})^2$  so the error in the DMR normalization of  $P(k)$  is approximately twice that in the DMR determination of  $Q_{\text{rms-PS}}$  (which is discussed below). As always, when comparing model predictions to observational measurements it is important to account for this normalization uncertainty, rather than basing conclusions about model viability solely on the “central” normalization value.

The mean square linear mass fluctuation averaged over a sphere of coordinate radius  $\bar{\chi}$  is

$$\left\langle \left[ \frac{\delta M}{M}(\bar{\chi}) \right]^2 \right\rangle = \frac{9}{2\pi^2} \int_0^\infty dk \frac{k^2 P(k)}{(k\bar{\chi})^6} [\sin(k\bar{\chi}) - k\bar{\chi} \cos(k\bar{\chi})]^2. \quad (5)$$

Tables 5–7 list predictions for  $(\delta M/M)(8h^{-1}\text{Mpc})$  or  $\sigma_8$ , the square root of the above expression evaluated at  $8h^{-1}\text{Mpc}$ , for various values of  $\alpha$  and  $\Omega_0$ . In Tables 5–7 we list the mean of the central values obtained from the foreground-emission-corrected quadrupole-included analysis and the foreground-emission-uncorrected quadrupole-excluded analysis.

Górski et al. (1998) show that the maximal  $1\sigma$  fractional  $Q_{\text{rms-PS}}$  (and so  $\delta M/M$ ) uncertainty from the DMR data ranges between about 10 % and 12 %, depending on model parameter values, and the maximal  $2\sigma$  uncertainty ranges between about 16 % and 19 %. As we have not done a complete analysis of all possible DMR data sets here, we adopt 10 % and 20 % as our  $1$  and  $2\sigma$  DMR normalization uncertainties for the dark energy scalar field models, for the purpose of comparing model predictions to observational measurements.

<sup>12</sup>Numerical noise and other small effects contribute to the tiny artificial differences between the various  $\Omega_0 = 1$  model predictions in this and other tables.

#### 4. Observational Constraints on DMR-Normalized Models

Given the dependence of the DMR likelihoods on the quadrupole moment of the CMB anisotropy, the DMR data do not meaningfully exclude any part of the  $(\Omega_0, \alpha, t_0, \Omega_B h^2)$  parameter space for the dark energy scalar field model considered here. In this section we combine current observational constraints on cosmological parameters (as summarized in Peebles & Ratra 2003; Chen & Ratra 2003b; Bennett et al. 2003a) with the DMR-normalized model predictions to place semi-quantitative constraints on the range of allowed model-parameter values.

We focus on the parameter values and predictions of Tables 5–7. These are computed for parameter values  $\Omega_B h^2 = 0.014$  and  $t_0 = 13$  Gyr (Table 5),  $\Omega_B h^2 = 0.006$  and  $t_0 = 11$  Gyr (Table 6), and  $\Omega_B h^2 = 0.022$  and  $t_0 = 17$  Gyr (Table 7), which span the two standard deviation range of interest:

$$11 \text{ Gyr} \leq t_0 \leq 17 \text{ Gyr}, \quad (6)$$

$$0.006 \leq \Omega_B h^2 \leq 0.022, \quad (7)$$

with central values of  $t_0 = 13$  Gyr and  $\Omega_B h^2 = 0.014$  (as summarized in Peebles & Ratra 2003). The recent WMAP measurements (Bennett et al. 2003a) lie in the center of the above  $t_0$  range,  $13.3 \text{ Gyr} \leq t_0 \leq 14.1 \text{ Gyr}$  ( $2\sigma$ ), and near the upper end of the above  $\Omega_B h^2$  range  $0.021 \leq \Omega_B h^2 \leq 0.024$  ( $2\sigma$ ), in good agreement with standard Big Bang nucleosynthesis theory and primordial deuterium abundance observations.

The first columns in Tables 5–7 list  $\Omega_0$ . A recent analysis of pre-WMAP constraints on  $\Omega_0$  from a combination of dynamical, baryon fraction, power spectrum, weak lensing, and cluster abundance measurements results in the two standard deviation range

$$0.2 \lesssim \Omega_0 \lesssim 0.35 \quad (8)$$

(Chen & Ratra 2003b), in striking accord with the Bennett et al. (2003a) WMAP estimate of  $0.19 \leq \Omega_0 \leq 0.35$  ( $2\sigma$ ). This constraint on  $\Omega_0$  significantly narrows the range of viable model-parameter values.

From an analysis of all available measurements of the Hubble parameter prior to mid 1999, Gott et al. (2001) find at two standard deviations

$$0.6 \leq h \leq 0.74, \quad (9)$$

with central value  $h = 0.67$ . This is in good agreement with the WMAP estimate  $0.65 \leq h \leq 0.79$  ( $2\sigma$ ) with central value  $h = 0.71$  (Bennett et al. 2003a). This constraint on  $h$  also significantly narrows the range of viable model parameters.

For an estimate of the rms linear fractional mass fluctuations at  $8h^{-1}$  Mpc we use, at  $2\sigma$ ,

$$0.72 \leq \sigma_8 \leq 1.16, \quad (10)$$

with  $\sigma_8 = 0.94$  as central value (Chen & Ratra 2003b), with an additional  $2\sigma$  DMR normalization uncertainty of 20 % added in quadrature.

Focussing on the numerical values of Tables 5–7, and combining the preceding constraints, there remains a small range of parameter space that is observationally viable. In particular, models with  $\Omega_0 \sim 0.3$  and  $\alpha$  ranging from 0 to  $\sim 3$  with  $\Omega_B h^2 = 0.014$  and  $t_0 = 13$  Gyr, are viable, while larger values of  $\Omega_B h^2 = 0.022$  and  $t_0 = 17$  Gyr narrow the range of  $\alpha$  significantly, barely allowing a constant  $\Lambda$  model with  $\alpha = 0$ .

Dark energy models that deviate significantly from Einstein’s cosmological constant are not favored by the data, i.e., the data favor  $\alpha$  closer to 0. A model with  $\alpha = 3$ , as is still allowed, requires new physics near a characteristic energy scale  $\sim 10^3$  GeV (Peebles & Ratra 1988, 2003), which should soon be probed by accelerator-based elementary particle physics experiments.

## 5. Conclusion

We have normalized the inverse-power-law-potential scalar field dark energy model by comparing the predicted CMB anisotropy in this model to that measured by the DMR experiment. In addition to effects associated with the DMR data — see Górski et al. (1998) for a more detailed discussion — the model normalization is sensitive to the values of  $\Omega_0$  and  $\alpha$  (the exponent of the inverse-power-law potential) but almost independent of the values of  $\Omega_B$  and  $h$ .

The DMR data alone can not be used to constrain  $\Omega_0$  and  $\alpha$  over the ranges considered here. Current cosmographic observations, in conjunction with current large-scale structure observations compared to the predictions of the DMR-normalized dark energy scalar field model, do however provide quite restrictive constraints on model parameter values. This is largely because  $\sigma_8$  depends sensitively on the values of  $\alpha$  and  $\Omega_0$  (see, e.g., Douspis et al. 2002), more so than the positions of the peaks in the CMB anisotropy spectrum.

As discussed in the previous section, there is a small range of model parameter values where evolving dark energy density models remain an observationally-viable alternative to a constant cosmological constant model, however, the data do not favor large deviations from the constant  $\Lambda$  model. It would therefore be of interest to examine more closely the supergravity-inspired generalization of the inverse-power-law-potential scalar field dark energy model (Brax & Martin 2000; Brax et al. 2000), which has a scalar field potential that results in a slower evolution of the dark energy density, more like a constant  $\Lambda$ .

It is possible that current or future WMAP (see, e.g., Bennett et al. 2003a) and other CMB anisotropy data will significantly circumscribe this option (see, e.g., Baccigalupi et al. 2002; Mukherjee et al. 2003a; Caldwell & Doran 2003), although it should be noted that the constraints derived here are quite restrictive since  $\sigma_8$  is very sensitive to the values of  $\alpha$  and  $\Omega_0$ . Among other experiments, the proposed SNAP space mission to measure the redshift-magnitude relation out to a redshift of two should also provide interesting constraints on evolving dark energy (see, e.g., Podariu, Nugent, & Ratra 2001a; Wang & Lovelace 2001; Weller & Albrecht 2002; Gerke & Efstathiou 2002; Eriksson & Amanullah 2002; Rhodes et al. 2003).

We acknowledge the advice and assistance of P. Brax, J. Lesgourgues, and J. Martin. PM and BR acknowledge support from NSF CAREER grant AST-9875031. This work was partially carried out at the Jet Propulsion Laboratory of the California Institute of Technology, under a contract with the National Aeronautics and Space Administration.

Table 1.  $Q_{\text{rms-PS}}$  Values for the  $t_0 = 13$  Gyr,  $\Omega_B h^2 = 0.014$  Models<sup>a</sup>

		$\alpha=0$		$\alpha=2$		$\alpha=4$		$\alpha=6$	
G.C. <sup>b</sup> : $\ell_{\text{min}}$ :	Yes	No	Yes	No	Yes	No	Yes	No	
	2	3	2	3	2	3	2	3	
$\Omega_0$	$h$	$Q_{\text{rms-PS}}$ ( $\mu\text{K}$ )							
(1)	(2)	(3)	(4)	(5)	(6)	(7)	(8)	(9)	(10)
0.1	0.96	22.52 <sub>21.00</sub> <sup>24.12</sup> 25.84	23.88 <sub>22.28</sub> <sup>25.52</sup> 27.36	24.76 <sub>23.04</sub> <sup>26.60</sup> 28.56	26.36 <sub>24.56</sub> <sup>28.24</sup> 30.28	26.68 <sub>24.84</sub> <sup>28.68</sup> 30.80	28.44 <sub>26.52</sub> <sup>30.48</sup> 32.64	28.44 <sub>26.44</sub> <sup>30.52</sup> 32.76	30.32 <sub>28.20</sub> <sup>32.36</sup> 34.64
0.2	0.81	20.20 <sub>18.84</sub> <sup>21.60</sup> 23.12	21.36 <sub>19.96</sub> <sup>22.88</sup> 24.40	22.52 <sub>20.96</sub> <sup>24.12</sup> 25.92	23.88 <sub>22.28</sub> <sup>25.56</sup> 27.40	24.32 <sub>22.68</sub> <sup>26.12</sup> 28.04	25.84 <sub>24.12</sub> <sup>27.72</sup> 29.72	25.76 <sub>23.96</sub> <sup>27.64</sup> 29.68	27.40 <sub>25.52</sub> <sup>29.32</sup> 31.44
0.3	0.72	18.80 <sub>17.56</sub> <sup>20.08</sup> 21.48	19.84 <sub>18.60</sub> <sup>21.20</sup> 22.64	20.56 <sub>19.20</sub> <sup>22.04</sup> 23.60	21.76 <sub>20.36</sub> <sup>23.28</sup> 24.92	22.20 <sub>20.72</sub> <sup>23.80</sup> 25.56	23.56 <sub>22.00</sub> <sup>25.20</sup> 27.00	23.44 <sub>21.84</sub> <sup>25.12</sup> 26.96	24.88 <sub>23.20</sub> <sup>26.60</sup> 28.52
0.4	0.67	17.96 <sub>16.80</sub> <sup>19.20</sup> 20.52	18.96 <sub>17.76</sub> <sup>20.24</sup> 21.60	18.84 <sub>17.60</sub> <sup>20.16</sup> 21.60	19.92 <sub>18.64</sub> <sup>21.28</sup> 22.76	20.16 <sub>18.84</sub> <sup>21.56</sup> 23.12	21.32 <sub>19.96</sub> <sup>22.80</sup> 24.40	21.16 <sub>19.76</sub> <sup>22.68</sup> 24.28	22.40 <sub>20.96</sub> <sup>23.96</sup> 25.64
0.5	0.62	17.40 <sub>16.28</sub> <sup>18.60</sup> 19.88	18.36 <sub>17.24</sub> <sup>19.60</sup> 20.92	17.52 <sub>16.40</sub> <sup>18.72</sup> 20.00	18.48 <sub>17.32</sub> <sup>19.72</sup> 21.08	18.20 <sub>17.00</sub> <sup>19.44</sup> 20.80	19.20 <sub>18.00</sub> <sup>20.52</sup> 21.92	18.92 <sub>17.68</sub> <sup>20.20</sup> 21.64	20.00 <sub>18.72</sub> <sup>21.36</sup> 22.80
0.6	0.59	17.12 <sub>16.04</sub> <sup>18.28</sup> 19.52	18.04 <sub>16.92</sub> <sup>19.24</sup> 20.56	16.48 <sub>15.44</sub> <sup>17.60</sup> 18.84	17.40 <sub>16.28</sub> <sup>18.52</sup> 19.80	16.52 <sub>15.48</sub> <sup>17.64</sup> 18.84	17.40 <sub>16.32</sub> <sup>18.56</sup> 19.84	16.80 <sub>15.72</sub> <sup>17.92</sup> 19.16	17.68 <sub>16.60</sub> <sup>18.88</sup> 20.12
0.7	0.56	16.96 <sub>15.88</sub> <sup>18.12</sup> 19.36	17.88 <sub>16.76</sub> <sup>19.08</sup> 20.36	15.96 <sub>14.92</sub> <sup>17.00</sup> 18.20	16.80 <sub>15.76</sub> <sup>17.92</sup> 19.08	15.44 <sub>14.48</sub> <sup>16.48</sup> 17.60	16.24 <sub>15.24</sub> <sup>17.32</sup> 18.48	15.16 <sub>14.20</sub> <sup>16.16</sup> 17.24	15.92 <sub>14.96</sub> <sup>16.96</sup> 18.12
0.8	0.54	16.96 <sub>15.84</sub> <sup>18.08</sup> 19.32	17.88 <sub>16.72</sub> <sup>19.04</sup> 20.32	15.88 <sub>14.88</sub> <sup>16.96</sup> 18.08	16.72 <sub>15.68</sub> <sup>17.80</sup> 19.00	15.08 <sub>14.12</sub> <sup>16.08</sup> 17.16	15.88 <sub>14.88</sub> <sup>16.88</sup> 18.04	14.48 <sub>13.60</sub> <sup>15.44</sup> 16.48	15.24 <sub>14.32</sub> <sup>16.24</sup> 17.32
0.9	0.52	16.96 <sub>15.88</sub> <sup>18.12</sup> 19.36	17.92 <sub>16.76</sub> <sup>19.08</sup> 20.36	16.32 <sub>15.28</sub> <sup>17.40</sup> 18.60	17.16 <sub>16.12</sub> <sup>18.32</sup> 19.56	15.64 <sub>14.68</sub> <sup>16.72</sup> 17.84	16.48 <sub>15.48</sub> <sup>17.56</sup> 18.72	15.24 <sub>14.28</sub> <sup>16.24</sup> 17.32	16.00 <sub>15.04</sub> <sup>17.08</sup> 18.20
1	0.50	17.04 <sub>15.96</sub> <sup>18.20</sup> 19.48	18.00 <sub>16.88</sub> <sup>19.20</sup> 20.48	17.08 <sub>16.00</sub> <sup>18.24</sup> 19.52	18.04 <sub>16.92</sub> <sup>19.20</sup> 20.52	17.04 <sub>15.96</sub> <sup>18.20</sup> 19.44	17.96 <sub>16.84</sub> <sup>19.16</sup> 20.44	17.04 <sub>15.96</sub> <sup>18.20</sup> 19.48	18.00 <sub>16.88</sub> <sup>19.20</sup> 20.48

<sup>a</sup>The tabulated  $Q_{\text{rms-PS}}$  values are determined from the conditional likelihood function at fixed  $\Omega_0$  and  $\alpha$ . At each  $\Omega_0$  and  $\alpha$ , the first of the five entries in each of columns (3)–(10) is the maximum likelihood value, the first (vertical) pair delimits the 68.3 % (1  $\sigma$ ) highest posterior density range, and the second (vertical) pair delimits the 95.5 % (2  $\sigma$ ) highest posterior density range.

<sup>b</sup>Accounting for (Yes), or ignoring (No) the correction for faint high-latitude foreground Galactic emission.

Table 2.  $Q_{\text{rms-PS}}$  Values for the  $t_0 = 11$  Gyr,  $\Omega_B h^2 = 0.006$  Models<sup>a</sup>

		$\alpha=0$		$\alpha=2$		$\alpha=4$		$\alpha=6$	
G.C. <sup>b</sup> : $\ell_{\text{min}}$ :	Yes	No	Yes	No	Yes	No	Yes	No	
	2	3	2	3	2	3	2	3	
$\Omega_0$	$h$	$Q_{\text{rms-PS}}$ ( $\mu\text{K}$ )							
(1)	(2)	(3)	(4)	(5)	(6)	(7)	(8)	(9)	(10)
0.1	1.13	22.72 <sup>24.36</sup> <sub>21.16</sub> <sup>26.12</sup> <sub>19.68</sub>	24.12 <sup>25.80</sup> <sub>22.52</sub> <sup>27.64</sup> <sub>20.96</sub>	24.96 <sup>26.84</sup> <sub>23.24</sub> <sup>28.84</sup> <sub>21.56</sub>	25.96 <sup>28.52</sup> <sub>24.76</sub> <sup>30.60</sup> <sub>23.04</sub>	26.96 <sup>28.96</sup> <sub>25.04</sub> <sup>31.16</sup> <sub>23.24</sub>	28.72 <sup>30.80</sup> <sub>26.76</sub> <sup>32.96</sup> <sub>24.84</sub>	28.76 <sup>30.92</sup> <sub>26.76</sub> <sup>33.16</sup> <sub>24.80</sub>	30.64 <sup>32.76</sup> <sub>28.56</sub> <sup>35.12</sup> <sub>26.52</sub>
0.2	0.96	20.36 <sup>21.80</sup> <sub>19.00</sub> <sup>23.36</sup> <sub>17.72</sub>	21.56 <sup>23.04</sup> <sub>20.16</sub> <sup>24.68</sup> <sub>18.84</sub>	22.68 <sup>24.32</sup> <sub>21.12</sub> <sup>26.12</sup> <sub>19.64</sub>	24.08 <sup>25.80</sup> <sub>22.48</sub> <sup>27.64</sup> <sub>20.92</sub>	24.56 <sup>26.36</sup> <sub>22.84</sub> <sup>28.32</sup> <sub>21.24</sub>	26.12 <sup>27.96</sup> <sub>24.32</sub> <sup>30.00</sup> <sub>22.64</sub>	26.00 <sup>27.96</sup> <sub>24.20</sub> <sup>30.04</sup> <sub>22.48</sub>	27.68 <sup>29.68</sup> <sub>25.80</sub> <sup>31.84</sup> <sub>24.04</sub>
0.3	0.86	18.96 <sup>20.28</sup> <sub>17.72</sub> <sup>21.72</sup> <sub>16.52</sub>	20.04 <sup>21.40</sup> <sub>18.76</sub> <sup>22.88</sup> <sub>17.56</sub>	20.76 <sup>22.24</sup> <sub>19.36</sub> <sup>23.84</sup> <sub>18.04</sub>	22.00 <sup>23.52</sup> <sub>20.56</sub> <sup>25.16</sup> <sub>19.16</sub>	22.44 <sup>24.04</sup> <sub>20.88</sub> <sup>25.80</sup> <sub>19.44</sub>	23.80 <sup>25.48</sup> <sub>22.24</sub> <sup>27.28</sup> <sub>20.68</sub>	23.64 <sup>25.36</sup> <sub>22.04</sub> <sup>27.24</sup> <sub>20.48</sub>	25.12 <sup>26.88</sup> <sub>23.48</sub> <sup>28.84</sup> <sub>21.84</sub>
0.4	0.79	18.12 <sup>19.36</sup> <sub>16.92</sub> <sup>20.72</sup> <sub>15.80</sub>	19.12 <sup>20.44</sup> <sub>17.92</sub> <sup>21.84</sup> <sub>16.76</sub>	19.04 <sup>20.36</sup> <sub>17.76</sub> <sup>21.80</sup> <sub>16.56</sub>	20.12 <sup>21.52</sup> <sub>18.84</sub> <sup>23.04</sup> <sub>17.60</sub>	20.36 <sup>21.80</sup> <sub>19.00</sub> <sup>23.32</sup> <sub>17.68</sub>	21.52 <sup>23.04</sup> <sub>20.16</sub> <sup>24.64</sup> <sub>18.80</sub>	21.36 <sup>22.88</sup> <sub>19.96</sub> <sup>24.52</sup> <sub>18.56</sub>	22.64 <sup>24.20</sup> <sub>21.16</sub> <sup>25.92</sup> <sub>19.76</sub>
0.5	0.74	17.60 <sup>18.80</sup> <sub>16.48</sub> <sup>20.12</sup> <sub>15.36</sub>	18.56 <sup>19.80</sup> <sub>17.40</sub> <sup>21.16</sup> <sub>16.24</sub>	17.68 <sup>18.88</sup> <sub>16.52</sub> <sup>20.24</sup> <sub>15.44</sub>	18.68 <sup>19.92</sup> <sub>17.48</sub> <sup>21.28</sup> <sub>16.32</sub>	18.36 <sup>19.64</sup> <sub>17.16</sub> <sup>21.00</sup> <sub>16.04</sub>	19.40 <sup>20.72</sup> <sub>18.16</sub> <sup>22.16</sup> <sub>16.96</sub>	19.12 <sup>20.44</sup> <sub>17.88</sub> <sup>21.88</sup> <sub>16.64</sub>	20.20 <sup>21.60</sup> <sub>18.92</sub> <sup>23.08</sup> <sub>17.68</sub>
0.6	0.70	17.28 <sup>18.44</sup> <sub>16.16</sub> <sup>19.72</sup> <sub>15.08</sub>	18.24 <sup>19.44</sup> <sub>17.08</sub> <sup>20.76</sup> <sub>15.96</sub>	16.60 <sup>17.76</sup> <sub>15.56</sub> <sup>19.00</sup> <sub>14.52</sub>	17.52 <sup>18.72</sup> <sub>16.44</sub> <sup>20.00</sup> <sub>15.36</sub>	16.68 <sup>17.80</sup> <sub>15.60</sub> <sup>19.04</sup> <sub>14.56</sub>	17.60 <sup>18.76</sup> <sub>16.48</sub> <sup>20.04</sup> <sub>15.40</sub>	16.96 <sup>18.12</sup> <sub>15.82</sub> <sup>19.36</sup> <sub>14.84</sub>	17.88 <sup>19.08</sup> <sub>16.76</sub> <sup>20.36</sup> <sub>15.68</sub>
0.7	0.66	17.12 <sup>18.24</sup> <sub>16.00</sub> <sup>19.56</sup> <sub>14.96</sub>	18.04 <sup>19.24</sup> <sub>16.92</sub> <sup>20.56</sup> <sub>15.80</sub>	16.08 <sup>17.20</sup> <sub>15.08</sub> <sup>18.36</sup> <sub>14.04</sub>	16.96 <sup>18.08</sup> <sub>15.88</sub> <sup>19.32</sup> <sub>14.88</sub>	15.60 <sup>16.64</sup> <sub>14.60</sub> <sup>17.76</sup> <sub>13.64</sub>	16.40 <sup>17.48</sup> <sub>15.36</sub> <sup>18.68</sup> <sub>14.40</sub>	15.28 <sup>16.32</sup> <sub>14.32</sub> <sup>17.44</sup> <sub>13.40</sub>	16.08 <sup>17.16</sup> <sub>15.12</sub> <sup>18.28</sup> <sub>14.12</sub>
0.8	0.64	17.08 <sup>18.24</sup> <sub>16.00</sub> <sup>19.48</sup> <sub>14.92</sub>	18.00 <sup>19.20</sup> <sub>16.88</sub> <sup>20.52</sup> <sub>15.80</sub>	16.04 <sup>17.12</sup> <sub>15.00</sub> <sup>18.28</sup> <sub>14.00</sub>	16.88 <sup>18.00</sup> <sub>15.84</sub> <sup>19.20</sup> <sub>14.80</sub>	15.24 <sup>16.24</sup> <sub>14.24</sub> <sup>17.36</sup> <sub>13.32</sub>	16.00 <sup>17.08</sup> <sub>15.04</sub> <sup>18.20</sup> <sub>14.04</sub>	14.64 <sup>15.60</sup> <sub>13.72</sub> <sup>16.68</sup> <sub>12.84</sub>	15.40 <sup>16.40</sup> <sub>14.44</sub> <sup>17.48</sup> <sub>13.52</sub>
0.9	0.61	17.12 <sup>18.32</sup> <sub>16.04</sub> <sup>19.56</sup> <sub>15.00</sub>	18.08 <sup>19.28</sup> <sub>16.92</sub> <sup>20.60</sup> <sub>15.84</sub>	16.44 <sup>17.56</sup> <sub>15.40</sub> <sup>18.76</sup> <sub>14.36</sub>	17.32 <sup>18.48</sup> <sub>16.24</sub> <sup>19.72</sup> <sub>15.20</sub>	15.80 <sup>16.88</sup> <sub>14.80</sub> <sup>18.00</sup> <sub>13.80</sub>	16.64 <sup>17.72</sup> <sub>15.60</sub> <sup>18.92</sup> <sub>14.60</sub>	15.36 <sup>16.40</sup> <sub>14.40</sub> <sup>17.48</sup> <sub>13.44</sub>	16.16 <sup>17.20</sup> <sub>15.16</sub> <sup>18.40</sup> <sub>14.20</sub>
1	0.59	17.20 <sup>18.40</sup> <sub>16.12</sub> <sup>19.64</sup> <sub>15.04</sub>	18.16 <sup>19.36</sup> <sub>17.00</sub> <sup>20.68</sup> <sub>15.92</sub>	17.24 <sup>18.40</sup> <sub>16.12</sub> <sup>19.68</sup> <sub>15.04</sub>	18.20 <sup>19.40</sup> <sub>17.04</sub> <sup>20.72</sup> <sub>15.96</sub>	17.16 <sup>18.36</sup> <sub>16.08</sub> <sup>19.60</sup> <sub>15.00</sub>	18.12 <sup>19.32</sup> <sub>16.96</sub> <sup>20.64</sup> <sub>15.88</sub>	17.20 <sup>18.40</sup> <sub>16.12</sub> <sup>19.64</sup> <sub>15.04</sub>	18.16 <sup>19.36</sup> <sub>17.00</sub> <sup>20.68</sup> <sub>15.92</sub>

<sup>a</sup>The tabulated  $Q_{\text{rms-PS}}$  values are determined from the conditional likelihood function at fixed  $\Omega_0$  and  $\alpha$ . At each  $\Omega_0$  and  $\alpha$ , the first of the five entries in each of columns (3)–(10) is the maximum likelihood value, the first (vertical) pair delimits the 68.3 % (1  $\sigma$ ) highest posterior density range, and the second (vertical) pair delimits the 95.5 % (2  $\sigma$ ) highest posterior density range.

<sup>b</sup>Accounting for (Yes), or ignoring (No) the correction for faint high-latitude foreground Galactic emission.

Table 3.  $Q_{\text{rms-PS}}$  Values for the  $t_0 = 17$  Gyr,  $\Omega_B h^2 = 0.022$  Models<sup>a</sup>

		$\alpha=0$		$\alpha=2$		$\alpha=4$		$\alpha=6$	
G.C. <sup>b</sup> : $\ell_{\text{min}}$ :	Yes	No	Yes	No	Yes	No	Yes	No	
	2	3	2	3	2	3	2	3	
$\Omega_0$	$h$	$Q_{\text{rms-PS}}$ ( $\mu\text{K}$ )							
(1)	(2)	(3)	(4)	(5)	(6)	(7)	(8)	(9)	(10)
0.1	0.73	22.20 <sup>23.76</sup> <sub>20.72</sub> <sup>25.44</sup> <sub>19.28</sub>	23.52 <sup>25.12</sup> <sub>21.96</sub> <sup>26.88</sup> <sub>20.52</sub>	24.48 <sup>26.28</sup> <sub>22.80</sub> <sup>28.20</sup> <sub>21.20</sub>	26.00 <sup>27.88</sup> <sub>24.28</sub> <sup>29.84</sup> <sub>22.60</sub>	26.24 <sup>28.20</sup> <sub>24.44</sub> <sup>30.28</sup> <sub>22.72</sub>	27.92 <sup>29.92</sup> <sub>26.04</sub> <sup>32.04</sup> <sub>24.28</sub>	27.84 <sup>29.92</sup> <sub>25.92</sub> <sup>32.08</sup> <sub>24.08</sub>	29.68 <sup>31.72</sup> <sub>27.68</sub> <sup>33.88</sup> <sub>25.76</sub>
0.2	0.62	19.88 <sup>21.24</sup> <sub>18.56</sub> <sup>22.76</sup> <sub>17.32</sub>	21.00 <sup>22.44</sup> <sub>19.68</sub> <sup>23.96</sup> <sub>18.40</sub>	22.28 <sup>23.84</sup> <sub>20.76</sub> <sup>25.60</sup> <sub>19.32</sub>	23.60 <sup>25.24</sup> <sub>22.04</sub> <sup>27.04</sup> <sub>20.56</sub>	24.04 <sup>25.08</sup> <sub>22.40</sub> <sup>27.68</sup> <sub>20.84</sub>	25.56 <sup>27.36</sup> <sub>23.84</sub> <sup>29.28</sup> <sub>22.24</sub>	25.36 <sup>27.20</sup> <sub>23.60</sub> <sup>29.20</sup> <sub>21.96</sub>	26.96 <sup>28.88</sup> <sub>25.16</sub> <sup>30.92</sup> <sub>23.44</sub>
0.3	0.55	18.60 <sup>19.88</sup> <sub>17.40</sub> <sup>21.24</sup> <sub>16.24</sub>	19.64 <sup>20.96</sup> <sub>18.40</sub> <sup>22.40</sup> <sub>17.20</sub>	20.36 <sup>21.76</sup> <sub>19.00</sub> <sup>23.36</sup> <sub>17.72</sub>	21.56 <sup>23.04</sup> <sub>20.16</sub> <sup>24.60</sup> <sub>18.80</sub>	21.96 <sup>23.52</sup> <sub>20.48</sub> <sup>25.24</sup> <sub>19.08</sub>	23.28 <sup>24.92</sup> <sub>21.76</sub> <sup>26.64</sup> <sub>20.28</sub>	23.08 <sup>24.76</sup> <sub>21.56</sub> <sup>26.52</sup> <sub>20.04</sub>	24.52 <sup>26.20</sup> <sub>22.88</sub> <sup>28.08</sup> <sub>21.36</sub>
0.4	0.51	17.76 <sup>19.00</sup> <sub>16.64</sub> <sup>20.28</sup> <sub>15.52</sub>	18.76 <sup>20.00</sup> <sub>17.56</sub> <sup>21.36</sup> <sub>16.44</sub>	18.68 <sup>20.00</sup> <sub>17.48</sub> <sup>21.36</sup> <sub>16.28</sub>	19.76 <sup>21.08</sup> <sub>18.48</sub> <sup>22.52</sup> <sub>17.28</sub>	19.92 <sup>21.32</sup> <sub>18.64</sub> <sup>22.84</sup> <sub>17.36</sub>	21.08 <sup>22.52</sup> <sub>19.72</sub> <sup>24.08</sup> <sub>18.44</sub>	20.88 <sup>22.36</sup> <sub>19.52</sub> <sup>23.92</sup> <sub>18.16</sub>	22.12 <sup>23.60</sup> <sub>20.68</sub> <sup>25.24</sup> <sub>19.28</sub>
0.5	0.48	17.20 <sup>18.36</sup> <sub>16.12</sub> <sup>19.64</sup> <sub>15.04</sub>	18.16 <sup>19.36</sup> <sub>17.04</sub> <sup>20.64</sup> <sub>15.92</sub>	17.32 <sup>18.48</sup> <sub>16.20</sub> <sup>19.76</sup> <sub>15.12</sub>	18.24 <sup>19.48</sup> <sub>17.12</sub> <sup>20.80</sup> <sub>16.00</sub>	18.00 <sup>19.24</sup> <sub>16.84</sub> <sup>20.56</sup> <sub>15.72</sub>	19.00 <sup>20.28</sup> <sub>17.80</sub> <sup>21.64</sup> <sub>16.64</sub>	18.68 <sup>19.92</sup> <sub>17.48</sub> <sup>21.32</sup> <sub>16.28</sub>	19.72 <sup>21.04</sup> <sub>18.48</sub> <sup>22.44</sup> <sub>17.28</sub>
0.6	0.45	16.96 <sup>18.12</sup> <sub>15.92</sub> <sup>19.36</sup> <sub>14.88</sub>	17.88 <sup>19.08</sup> <sub>16.80</sub> <sup>20.36</sup> <sub>15.72</sub>	16.32 <sup>17.40</sup> <sub>15.28</sub> <sup>18.60</sup> <sub>14.28</sub>	17.20 <sup>18.32</sup> <sub>16.12</sub> <sup>19.56</sup> <sub>15.08</sub>	16.36 <sup>17.44</sup> <sub>15.32</sub> <sup>18.68</sup> <sub>14.32</sub>	17.24 <sup>18.36</sup> <sub>16.16</sub> <sup>19.60</sup> <sub>15.12</sub>	16.56 <sup>17.68</sup> <sub>15.52</sub> <sup>18.92</sup> <sub>14.52</sub>	17.48 <sup>18.60</sup> <sub>16.36</sub> <sup>19.84</sup> <sub>15.32</sub>
0.7	0.43	16.76 <sup>17.92</sup> <sub>15.72</sub> <sup>19.12</sup> <sub>14.68</sub>	17.68 <sup>18.84</sup> <sub>16.56</sub> <sup>20.12</sup> <sub>15.52</sub>	15.80 <sup>16.88</sup> <sub>14.84</sub> <sup>18.04</sup> <sub>13.84</sub>	16.64 <sup>17.76</sup> <sub>15.64</sub> <sup>18.92</sup> <sub>14.60</sub>	15.28 <sup>16.28</sup> <sub>14.32</sub> <sup>17.36</sup> <sub>13.36</sub>	16.04 <sup>17.08</sup> <sub>15.04</sub> <sup>18.24</sup> <sub>14.12</sub>	14.96 <sup>15.92</sup> <sub>14.00</sub> <sup>17.00</sup> <sub>13.12</sub>	15.72 <sup>16.72</sup> <sub>14.76</sub> <sup>17.84</sup> <sub>13.80</sub>
0.8	0.41	16.80 <sup>17.92</sup> <sub>15.72</sub> <sup>19.12</sup> <sub>14.68</sub>	17.68 <sup>18.84</sup> <sub>16.60</sub> <sup>20.12</sup> <sub>15.52</sub>	15.72 <sup>16.80</sup> <sub>14.76</sub> <sup>17.92</sup> <sub>13.76</sub>	16.56 <sup>17.64</sup> <sub>15.52</sub> <sup>18.84</sup> <sub>14.56</sub>	14.96 <sup>15.96</sup> <sub>14.04</sub> <sup>17.04</sup> <sub>13.12</sub>	15.72 <sup>16.76</sup> <sub>14.76</sub> <sup>17.88</sup> <sub>13.84</sub>	14.32 <sup>15.28</sup> <sub>13.44</sub> <sup>16.28</sup> <sub>12.60</sub>	15.08 <sup>16.04</sup> <sub>14.16</sub> <sup>17.08</sup> <sub>13.24</sub>
0.9	0.40	16.84 <sup>17.96</sup> <sub>15.76</sub> <sup>19.20</sup> <sub>14.72</sub>	17.76 <sup>18.92</sup> <sub>16.64</sub> <sup>20.16</sup> <sub>15.56</sub>	16.16 <sup>17.24</sup> <sub>15.16</sub> <sup>18.44</sup> <sub>14.16</sub>	17.00 <sup>18.12</sup> <sub>15.96</sub> <sup>19.36</sup> <sub>14.96</sub>	15.52 <sup>16.56</sup> <sub>14.56</sub> <sup>17.68</sup> <sub>13.60</sub>	16.36 <sup>17.40</sup> <sub>15.32</sub> <sup>18.56</sup> <sub>14.36</sub>	15.04 <sup>16.00</sup> <sub>14.08</sub> <sup>17.08</sup> <sub>13.16</sub>	15.80 <sup>16.84</sup> <sub>14.84</sub> <sup>17.92</sup> <sub>13.88</sub>
1	0.38	16.84 <sup>18.04</sup> <sub>15.84</sub> <sup>19.28</sup> <sub>14.80</sub>	17.84 <sup>19.00</sup> <sub>16.72</sub> <sup>20.28</sup> <sub>15.64</sub>	16.92 <sup>18.08</sup> <sub>15.88</sub> <sup>19.32</sup> <sub>14.84</sub>	17.84 <sup>19.00</sup> <sub>16.72</sub> <sup>20.28</sup> <sub>15.64</sub>	16.92 <sup>18.04</sup> <sub>15.84</sub> <sup>19.28</sup> <sub>14.80</sub>	17.80 <sup>19.00</sup> <sub>16.72</sub> <sup>20.28</sup> <sub>15.64</sub>	16.92 <sup>18.08</sup> <sub>15.88</sub> <sup>19.32</sup> <sub>14.84</sub>	17.84 <sup>19.04</sup> <sub>16.76</sub> <sup>20.32</sup> <sub>15.68</sub>

<sup>a</sup>The tabulated  $Q_{\text{rms-PS}}$  values are determined from the conditional likelihood function at fixed  $\Omega_0$  and  $\alpha$ . At each  $\Omega_0$  and  $\alpha$ , the first of the five entries in each of columns (3)–(10) is the maximum likelihood value, the first (vertical) pair delimits the 68.3 % (1  $\sigma$ ) highest posterior density range, and the second (vertical) pair delimits the 95.5 % (2  $\sigma$ ) highest posterior density range.

<sup>b</sup>Accounting for (Yes), or ignoring (No) the correction for faint high-latitude foreground Galactic emission.

Table 4. Fractional Energy-Density Perturbation Power Spectrum Normalization Factor  $Ah^4$ <sup>a</sup>

$\Omega_0$	$\alpha=0$		$\alpha=2$		$\alpha=4$		$\alpha=6$	
	$Ah^4$		$Ah^4$		$Ah^4$		$Ah^4$	
	$(10^5 \text{ Mpc}^4)$		$(10^5 \text{ Mpc}^4)$		$(10^5 \text{ Mpc}^4)$		$(10^5 \text{ Mpc}^4)$	
(1)	(2)		(3)		(4)		(5)	
0.1	153 (28.4)		307 (47.0)		525 (69.1)		802 (92.9)	
0.2	62.9 (14.6)		125 (23.2)		208 (33.1)		303 (42.9)	
0.3	36.7 (9.82)		63.2 (14.1)		101 (19.3)		141 (24.2)	
0.4	24.8 (7.28)		34.3 (9.14)		50.3 (11.7)		66.8 (14.1)	
0.5	18.0 (5.64)		19.9 (6.14)		25.0 (7.16)		30.8 (8.13)	
0.6	13.8 (4.48)		12.4 (4.31)		12.9 (4.49)		13.9 (4.69)	
0.7	11.0 (3.62)		8.62 (3.21)		7.56 (3.01)		6.92 (2.87)	
0.8	8.99 (2.96)		6.89 (2.59)		5.51 (2.30)		4.55 (2.06)	
0.9	7.46 (2.45)		6.29 (2.24)		5.28 (2.05)		4.58 (1.88)	
1	6.29 (2.05)		6.31 (2.05)		6.27 (2.05)		6.29 (2.05)	

<sup>a</sup>Normalized to the mean of the central  $Q_{\text{rms-PS}}$  in the foreground-emission-corrected quadrupole-included and the foreground-emission-un-corrected quadrupole-excluded cases (normalized to  $Q_{\text{rms-PS}} = 10 \mu\text{K}$ ); scale as  $(Q_{\text{rms-PS}})^2$ . These are for the  $t_0 = 13$  Gyr and  $\Omega_B h^2 = 0.014$  models and are insensitive to the values of these parameters.

Table 5.  $(\delta M/M)(8h^{-1}\text{Mpc})$  for the  $t_0 = 13$  Gyr,  $\Omega_B h^2 = 0.014$  Models<sup>a</sup>

$\Omega_0$ (1)	$h$ (2)	$\alpha=0$	$\alpha=2$	$\alpha=4$	$\alpha=6$
		$\sigma_8$ (3)	$\sigma_8$ (4)	$\sigma_8$ (5)	$\sigma_8$ (6)
0.1	0.96	0.632	0.295	0.169	0.107
0.2	0.81	0.888	0.509	0.332	0.234
0.3	0.72	1.02	0.670	0.479	0.363
0.4	0.67	1.10	0.798	0.617	0.495
0.5	0.62	1.14	0.906	0.745	0.633
0.6	0.59	1.17	0.991	0.863	0.771
0.7	0.56	1.18	1.06	0.972	0.905
0.8	0.54	1.18	1.11	1.06	1.02
0.9	0.52	1.18	1.15	1.12	1.11
1	0.50	1.17	1.17	1.17	1.17

<sup>a</sup>The mean of the central values obtained from the foreground-emission-corrected quadrupole-included analysis and the foreground-emission-uncorrected quadrupole-excluded analysis

Table 6.  $(\delta M/M)(8h^{-1}\text{Mpc})$  for the  $t_0 = 11$  Gyr,  $\Omega_B h^2 = 0.006$  Models<sup>a</sup>

$\Omega_0$ (1)	$h$ (2)	$\alpha=0$	$\alpha=2$	$\alpha=4$	$\alpha=6$
		$\sigma_8$ (3)	$\sigma_8$ (4)	$\sigma_8$ (5)	$\sigma_8$ (6)
0.1	1.13	0.964	0.477	0.283	0.185
0.2	0.96	1.26	0.746	0.498	0.356
0.3	0.86	1.41	0.945	0.685	0.522
0.4	0.79	1.49	1.10	0.854	0.689
0.5	0.74	1.52	1.22	1.01	0.862
0.6	0.70	1.54	1.31	1.15	1.03
0.7	0.66	1.54	1.39	1.28	1.19
0.8	0.64	1.53	1.44	1.38	1.33
0.9	0.61	1.51	1.47	1.44	1.44
1	0.59	1.49	1.49	1.49	1.49

<sup>a</sup>The mean of the central values obtained from the foreground-emission-corrected quadrupole-included analysis and the foreground-emission-uncorrected quadrupole-excluded analysis.

Table 7.  $(\delta M/M)(8h^{-1}\text{Mpc})$  for the  $t_0 = 17$  Gyr,  $\Omega_B h^2 = 0.022$  Models<sup>a</sup>

$\Omega_0$ (1)	$h$ (2)	$\alpha=0$	$\alpha=2$	$\alpha=4$	$\alpha=6$
		$\sigma_8$ (3)	$\sigma_8$ (4)	$\sigma_8$ (5)	$\sigma_8$ (6)
0.1	0.73	0.273	0.107	0.0540	0.0316
0.2	0.62	0.453	0.241	0.149	0.101
0.3	0.55	0.562	0.352	0.244	0.179
0.4	0.51	0.631	0.445	0.336	0.265
0.5	0.48	0.675	0.523	0.425	0.356
0.6	0.45	0.707	0.589	0.509	0.450
0.7	0.43	0.724	0.645	0.588	0.544
0.8	0.41	0.740	0.689	0.655	0.629
0.9	0.40	0.748	0.725	0.709	0.698
1	0.38	0.751	0.751	0.750	0.751

<sup>a</sup>The mean of the central values obtained from the foreground-emission-corrected quadrupole-included analysis and the foreground-emission-uncorrected quadrupole-excluded analysis.

## REFERENCES

Alam, U., Sahni, V., & Starobinsky, A. A. 2003, astro-ph/0302302

Baccigalupi, C., Balbi, A., Matarrese, S., Perrotta, F., & Vittorio, N. 2002, Phys. Rev. D, 65, 063520

Banday, A. J., Dickinson, C., Davies, R. D., Davis, R. J., & Górski, K. M. 2003, astro-ph/0302181

Banday, A. J., et al. 1997, ApJ, 475, 393

Bennett, C. L., et al. 1996, ApJ, 464, L1

Bennett, C. L., et al. 2003a, astro-ph/0302207

Bennett, C. L., et al. 2003b, astro-ph/0302208

Brax, P., & Martin, J. 2000, Phys. Rev. D, 61, 103502

Brax, P., Martin, J., & Riazuelo, A. 2000, Phys. Rev. D, 62, 103505

Caldwell, R. R., & Doran, M. 2003, astro-ph/0305334

Caldwell, R. R., Kamionkowski, M., & Weinberg, N. N. 2003, astro-ph/0302506

Carroll, S. M., Hoffmann, M., & Trodden, M. 2003, astro-ph/0301273

Chae, K.-H., et al. 2002, Phys. Rev. Lett., 89, 151301

Chen, G., & Ratra, B. 2003a, ApJ, 582, 586

Chen, G., & Ratra, B. 2003b, PASP, in press, astro-ph/0302002

Daly, R. A., & Djorgovski, S. G.. 2003, astro-ph/0305197

De Troia, G., et al. 2003, astro-ph/0301294

Douspis, M., Riazuelo, A., Zolnierowski, Y., & Blanchard, A. 2002, astro-ph/0212097

Durrer, R., Novosyadlyj, B., & Apuneych, S. 2003, ApJ, 583, 33

Dvali, G., & Turner, M. S. 2003, astro-ph/0301510

Eriksson, M., & Amanullah, R. 2002, Phys. Rev. D, 66, 023530

Fischler, W., Ratra, B., & Susskind, L. 1985, Nucl. Phys. B, 259, 730

Gerke, B., & Efstathiou, G. 2002, MNRAS, 335, 33

Górski, K. M. 1994, ApJ, 430, L85

Górski, K. M., et al. 1996, ApJ, 464, L11

Górski, K. M., Ratra, B., Stompor, R., Sugiyama, N., & Banday, A. J. 1998, ApJS, 114, 1

Górski, K. M., Ratra, B., Sugiyama, N., & Banday, A. J. 1995, ApJ, 444, L65

Gott, J. R. 1982, Nature, 295, 304

Gott, J. R., Vogeley, M. S., Podariu, S., & Ratra, B. 2001, ApJ, 549, 1

Hamilton, A. J. S., Tegmark, M., & Padmanabhan, N. 2000, MNRAS, 317, L23

Harrison, E. R. 1970, Phys. Rev. D, 1, 2726

Hauser, M. G., Kelsall, T., Leisawitz, D., & Weiland, J. 1998, *COBE Diffuse Infrared Background Experiment (DIRBE) Explanatory Supplement*

Hu, W., & Dodelson, S. 2002, ARA&A, 40, 171

Jain, D., Dev, A., & Alcaniz, J. S. 2003, astro-ph/0302025

Kelsall, T., et al. 1998, ApJ, 508, 44

Klypin, A., Macciò, A. V., Mainini, R., & Bonometto, S. A. 2003, astro-ph/0303304

Komatsu, E., et al. 2003, astro-ph/0302223

Komatsu, E., Wandelt, B. D., Spergel, D. N., Banday, A. J., & Górski, K. M. 2002, ApJ, 566, 19

Leibundgut, B. 2001, ARA&A, 39, 67

Melchiorri, A., & Ödman, C. J. 2003, astro-ph/0302361

Mukherjee, P., Coble, K., Dragovan, M., Ganga, K., Kovac, J., Ratra, B., & Souradeep, T. 2003b, ApJ, in press, astro-ph/0301581

Mukherjee, P., Dennison, B., Ratra, B., Simonetti, J. H., Ganga, K., & Hamilton, J.-Ch. 2002, ApJ, 579, 83

Mukherjee, P., Ganga, K., Ratra, B., Rocha, G., Souradeep, T., Sugiyama, N., & Górski, K. M. 2003a, *Intl. J. Mod. Phys.*, in press, astro-ph/0209567

Mukherjee, P., Hobson, M. P., & Lasenby, A. N. 2000, MNRAS, 318, 1157

Munshi, D., Porciani, C., & Wang, Y. 2003, astro-ph/0302510

Padmanabhan, T. 2003, Phys. Repts., in press

Page, L., et al. 2003, astro-ph/0302220

Park, C.-G., Park, C., Ratra, B., & Tegmark, M. 2001, ApJ, 556, 582

Peebles, P. J. E. 1984, ApJ, 284, 439

Peebles, P. J. E., & Ratra, B. 1988, ApJ, 325, L17

Peebles, P. J. E., & Ratra, B. 2003, Rev. Mod. Phys., 75, 559

Peebles, P. J. E., & Yu, J. T. 1970, ApJ, 162, 815

Percival, W., et al. 2001, MNRAS, 327, 1297

Podariu, S., Daly, R. A., Mory, M. P., & Ratra, B. 2003, ApJ, 584, 577

Podariu, S., Nugent, P., & Ratra, B. 2001a, ApJ, 553, 39

Podariu, S., & Ratra, B. 2000, ApJ, 532, 109

Podariu, S., Souradeep, T., Gott, J. R., Ratra, B., & Vogeley, M. S. 2001b, ApJ, 559, 9

Ratra, B. 1985, Phys. Rev. D, 31, 1931

Ratra, B. 1991, Phys. Rev. D, 43, 3802

Ratra, B., & Peebles, P. J. E. 1988, Phys. Rev. D, 37, 3406

Ratra, B., & Peebles, P. J. E. 1995, Phys. Rev. D, 52, 1837

Ratra, B., & Quillen, A. 1992, MNRAS, 259, 738

Rhodes, J., et al. 2003, astro-ph/0304417

Rosati, F. 2003, hep-ph/0302159

Saini, T. D., Padmanabhan, T., & Bridle, S. 2003, MNRAS, in press

Santos, M. G., et al. 2002, Phys. Rev. Lett., 88, 241302

Sen, A. A., & Sen, S. 2003, astro-ph/0303383

Silva, P. T., & Bertolami, O. 2003, astro-ph/0303353

Singh, P., Sami, M., & Dadhich, N. 2003, hep-th/0305110

Spergel, D. N., et al. 2003, astro-ph/0302209

Tonry, J. L., et al. 2003, astro-ph/0305008

Waga, I., & Frieman, J. A. 2000, Phys. Rev. D, 62, 043521

Wang, Y., & Lovelace, G. 2001, ApJ, 562, L115

Weller, J., & Albrecht, A. 2002, Phys. Rev. D, 65, 103512

Wetterich, C. 2003, hep-ph/0301261

Zel'dovich, Ya. B. 1972, MNRAS, 160, 1P

Zhu, Z.-H., & Fujimoto, M.-K. 2003, ApJ, 585, 52

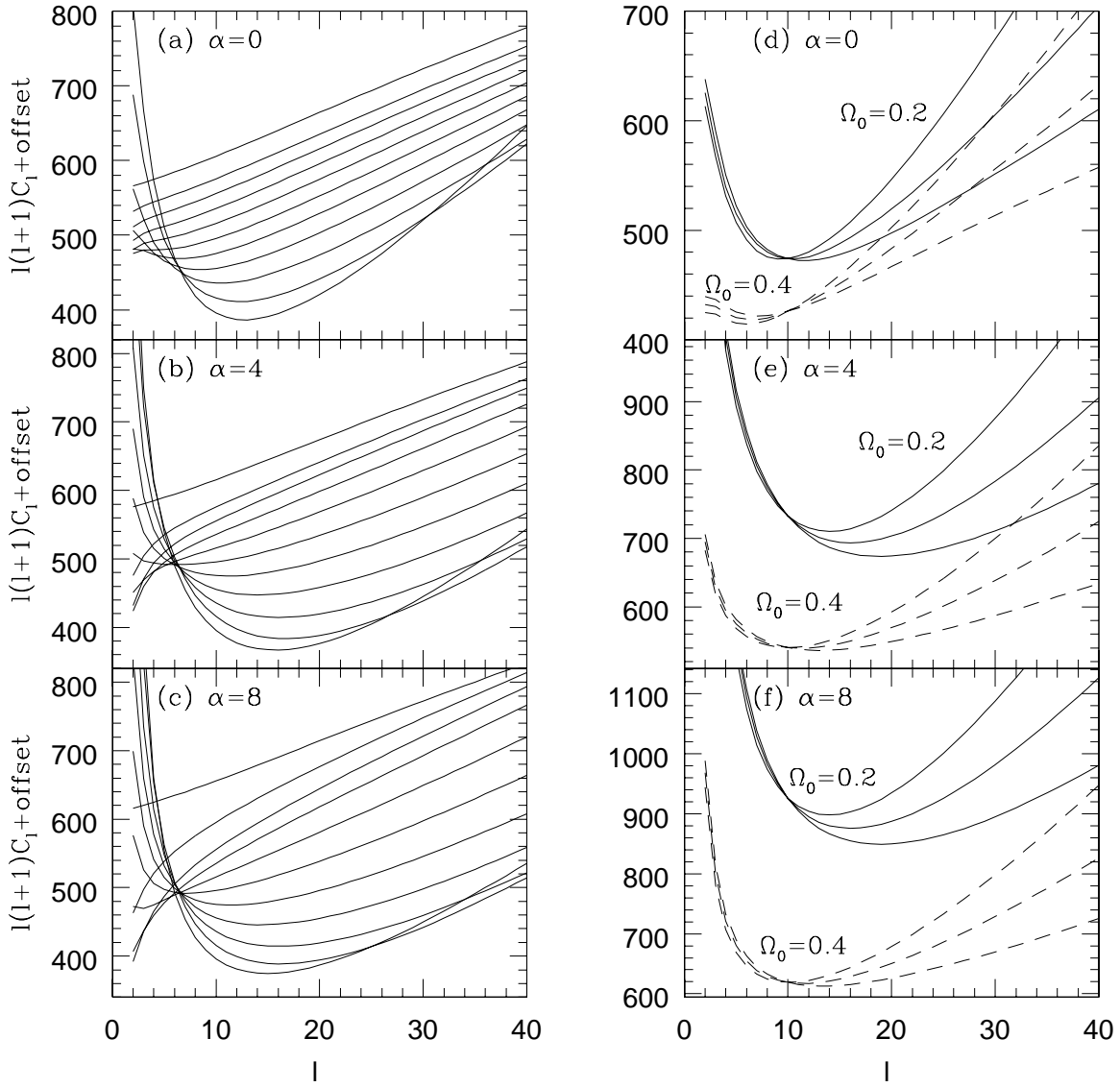


Fig. 1.— CMB anisotropy multipole coefficients. Panels *a*) and *d*) in the first row, *b*) and *e*) in the second row, and *c*) and *f*) in the third row correspond to models with  $\alpha = 0, 4$ , and  $8$ , respectively. Panels *a*), *b*), and *c*) in the left column show multipoles for a model with  $t_0 = 13$  Gyr and  $\Omega_B h^2 = 0.014$ . The coefficients are normalized relative to the  $C_9$  amplitude, and different values of  $\Omega_0$  are offset from each other to aid visualization. In each of these panels, at  $\ell = 9$ , the 11 curves, in ascending order, correspond to models with  $\Omega_0 = 0.05, 0.1, 0.2, \dots, 0.9, 1.0$ . The three panels in the right column show models with  $\Omega_0 = 0.2$  (solid curves) and  $0.4$  (dashed curves). Each set of three curves in these panels correspond, in ascending order on the right vertical axis of each panel, to models with parameter values  $(t_0, \Omega_B h^2) = (11 \text{ Gyr}, 0.006)$ ,  $(13 \text{ Gyr}, 0.014)$ , and  $(17 \text{ Gyr}, 0.022)$ , respectively.

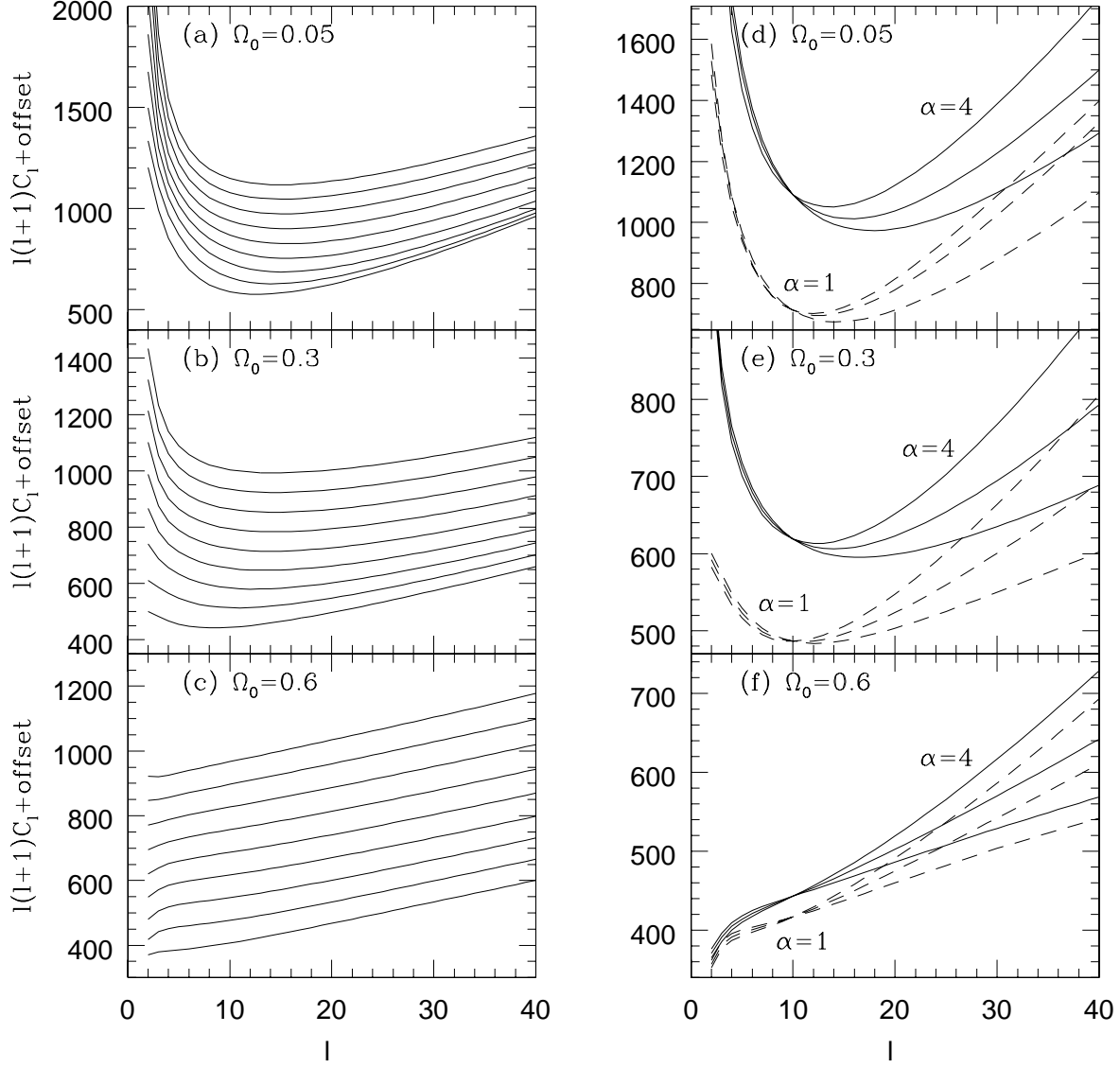


Fig. 2.— CMB anisotropy multipole coefficients. Panels *a*) and *d*) in the first row, *b*) and *e*) in the second row, and *c*) and *f*) in the third row correspond to models with  $\Omega_0 = 0.05, 0.3$ , and  $0.6$ , respectively. Panels *a*), *b*), and *c*) in the left column show multipoles for a model with  $t_0 = 13$  Gyr and  $\Omega_B h^2 = 0.014$ . The coefficients are normalized relative to the  $C_9$  amplitude, and different values of  $\alpha$  are offset from each other to aid visualization. In each of these panels, at  $\ell = 9$ , the 9 curves, in ascending order, correspond to models with  $\alpha = 0, 1, 2, \dots, 7, 8$ . The three panels in the right column show models with  $\alpha = 4$  (solid curves) and  $1$  (dashed curves). Each set of three curves in these panels correspond, in ascending order on the right vertical axis of each panel, to models with parameter values  $(t_0, \Omega_B h^2) = (11 \text{ Gyr}, 0.006), (13 \text{ Gyr}, 0.014)$ , and  $(17 \text{ Gyr}, 0.022)$ , respectively.

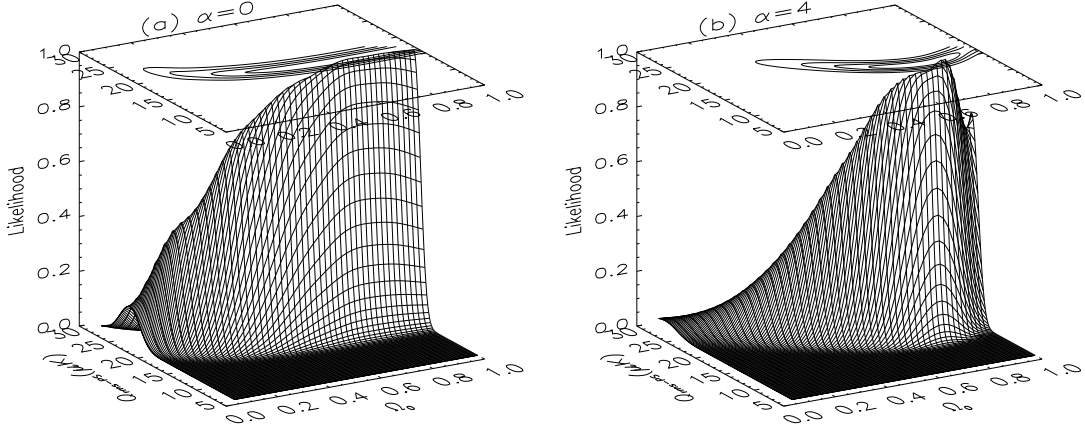


Fig. 3.— Likelihood functions  $L(Q_{\text{rms-PS}}, \Omega_0)$  (arbitrarily normalized to unity at the highest peak) derived from a simultaneous analysis of the DMR 53 and 90 GHz galactic-frame data, corrected for faint high-latitude foreground Galactic emission, and including the quadrupole moment in the analysis. These are for the model with  $t_0 = 13$  Gyr and  $\Omega_B h^2 = 0.014$ . Panel *a*) is for  $\alpha = 0$  and panel *b*) for  $\alpha = 4$ .

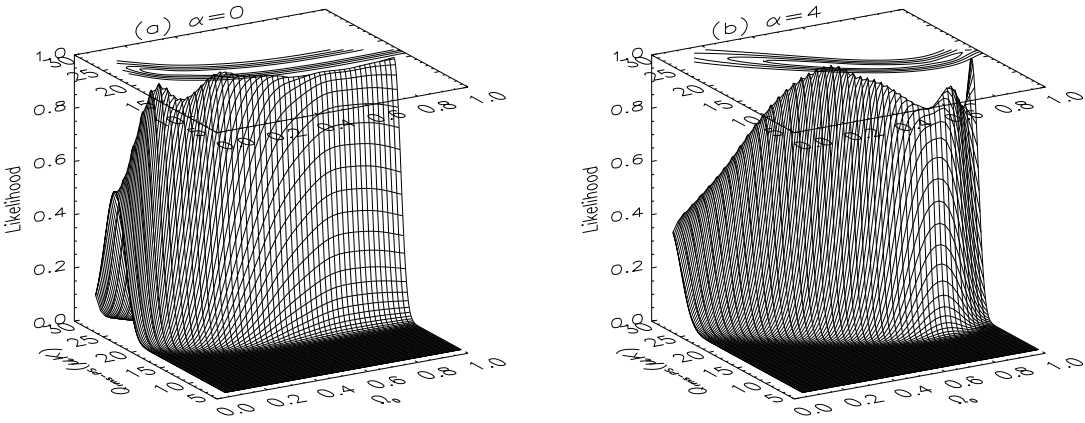


Fig. 4.— Likelihood functions  $L(Q_{\text{rms-PS}}, \Omega_0)$  (arbitrarily normalized to unity at the highest peak) derived from a simultaneous analysis of the DMR 53 and 90 GHz galactic-frame data, ignoring the correction for faint high-latitude foreground Galactic emission, and excluding the quadrupole moment from the analysis. These are for the model with  $t_0 = 13$  Gyr and  $\Omega_B h^2 = 0.014$ . Panel *a*) is for  $\alpha = 0$  and panel *b*) for  $\alpha = 4$ .

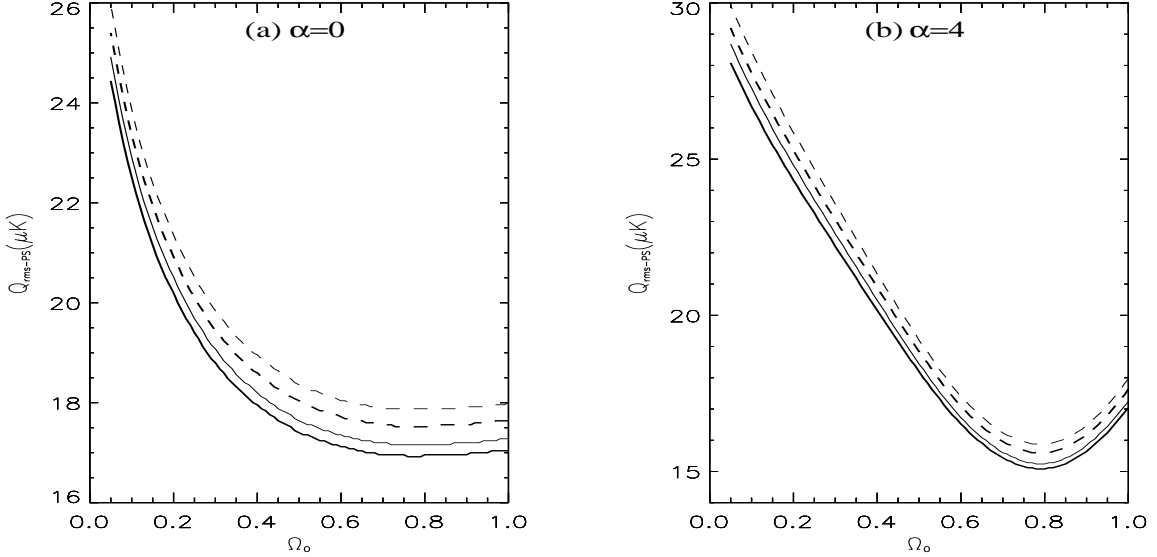


Fig. 5.— Ridge lines of the maximum likelihood  $Q_{\text{rms-PS}}$  value as a function of  $\Omega_0$ , for a)  $\alpha = 0$  and b)  $\alpha = 4$ . These are for the model with  $t_0 = 13$  Gyr and  $\Omega_B h^2 = 0.014$ . Four curves are shown in each panel: solid (dashed) curves correspond to accounting for (ignoring) the faint high-latitude foreground Galactic emission correction, while heavy (light) curves include (exclude) the quadrupole moment in the analysis.

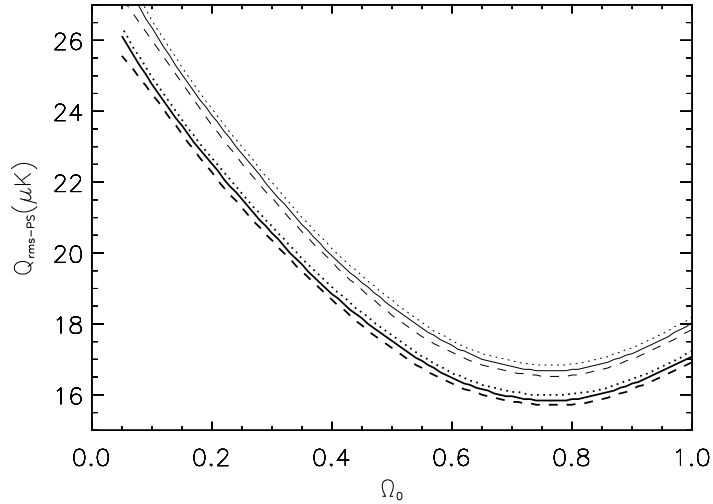


Fig. 6.— Ridge lines of the maximum likelihood  $Q_{\text{rms-PS}}$  value as a function of  $\Omega_0$ , for  $\alpha = 2$ . Six curves are shown. These correspond to parameter values  $(t_0, \Omega_B h^2) = (11 \text{ Gyr}, 0.006)$  (dotted curves),  $(13 \text{ Gyr}, 0.014)$  (solid curves), and  $(17 \text{ Gyr}, 0.022)$  (dashed curves). Heavy curves are determined by accounting for faint high-latitude foreground Galactic emission and including the quadrupole moment in the analysis, while light curves ignore the correction for faint high-latitude foreground Galactic emission and exclude the quadrupole moment from the analysis.

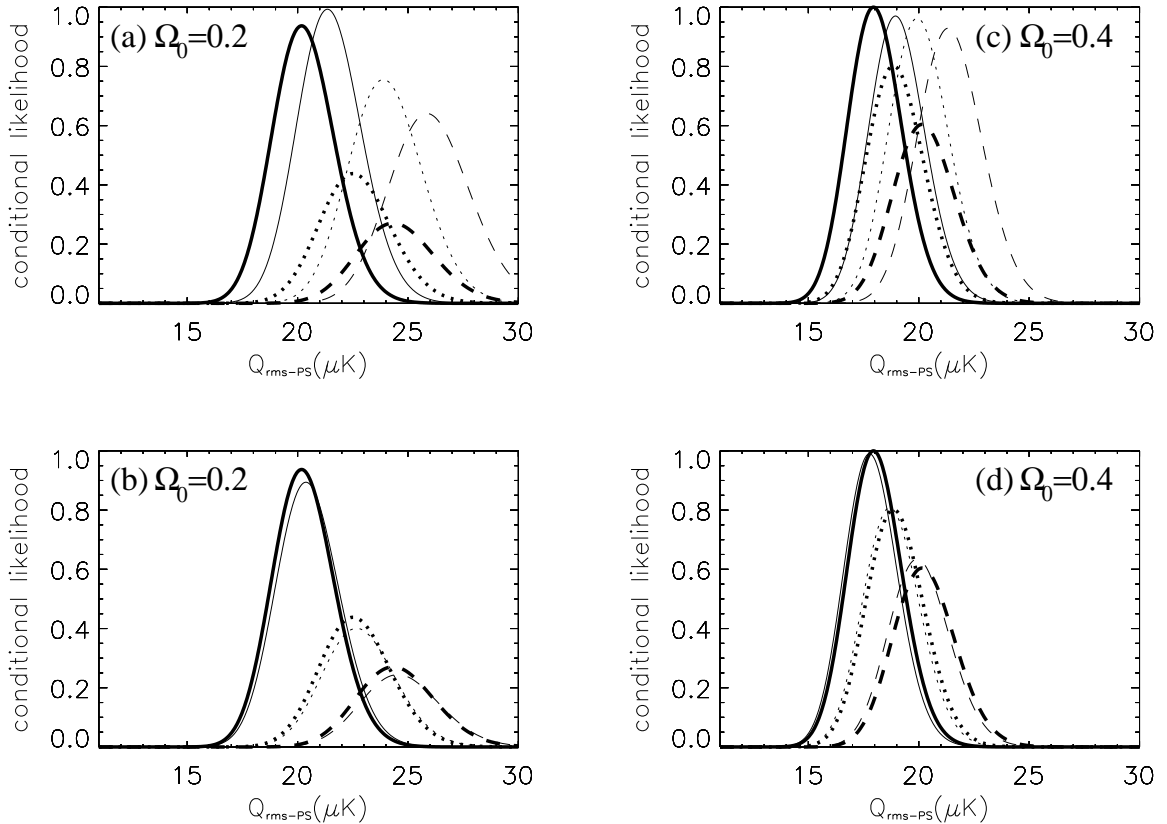


Fig. 7.— Conditional likelihood densities for  $Q_{\text{rms-PS}}$ , derived from  $L(Q_{\text{rms-PS}}, \Omega_0, \alpha)$  (which are normalized to be unity at the peak, for each DMR data set and set of model-parameter values). Left column panels *a*) and *b*) are for  $\Omega_0 = 0.2$  and right column panels *c*) and *d*) correspond to  $\Omega_0 = 0.4$ . Six curves are shown in each panel. Solid, dotted, and dashed curves correspond to  $\alpha = 0, 2$ , and  $4$ , respectively. In each panel, heavy curves are for a nominal model with  $t_0 = 13$  Gyr and  $\Omega_B h^2 = 0.014$  and are derived from the foreground-corrected quadrupole-included analysis. In the two upper panels the three light curves differ from the nominal heavy curves by not accounting for the faint high-latitude foreground Galactic emission correction and by excluding the quadrupole from the analysis. In the two lower panels the three light curves differ from the nominal ones by corresponding to models with  $t_0 = 11$  Gyr and  $\Omega_B h^2 = 0.006$  (panel *b*) on the left) and with  $t_0 = 17$  Gyr and  $\Omega_B h^2 = 0.022$  (panel *d*) on the right).

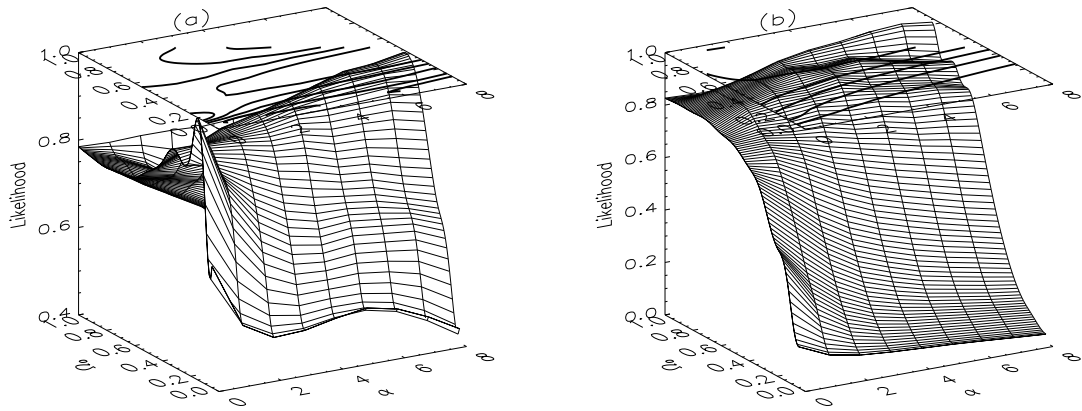


Fig. 8.— Likelihood functions  $L(\alpha, \Omega_0)$  (arbitrarily normalized to unity at the highest peak) derived by marginalizing  $L(Q_{\text{rms-PS}}, \alpha, \Omega_0)$  over  $Q_{\text{rms-PS}}$  with a uniform prior. These are for the model with  $t_0 = 13$  Gyr and  $\Omega_B h^2 = 0.014$ . Panel *a*) ignores the correction for faint high-latitude foreground Galactic emission and excludes the quadrupole moment from the analysis, while panel *b*) corrects for faint high-latitude foreground Galactic emission and includes the quadrupole moment in the analysis.

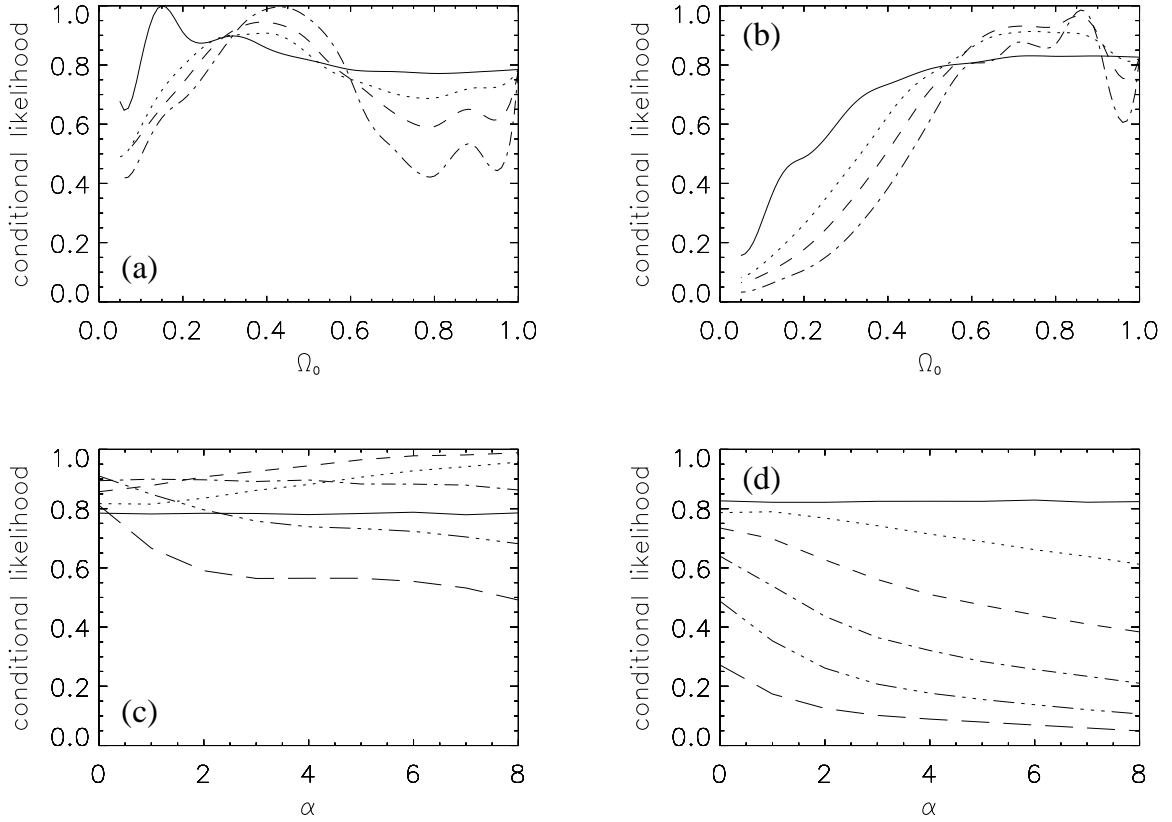


Fig. 9.— Conditional likelihood functions derived from  $L(\alpha, \Omega_0)$  (arbitrarily normalized to unity at the highest peak), which is derived by marginalizing  $L(Q_{\text{rms-PS}}, \alpha, \Omega_0)$  over  $Q_{\text{rms-PS}}$  with a uniform prior. These are for the model with  $t_0 = 13$  Gyr and  $\Omega_B h^2 = 0.014$ . Panels *a*) and *c*) in the left column ignore the correction for faint high-latitude foreground Galactic emission and exclude the quadrupole moment from the analysis. Panels *b*) and *d*) in the right column account for the correction for faint high-latitude foreground Galactic emission and include the quadrupole moment in the analysis. The top two panels show  $L(\Omega_0)$  on four constant  $\alpha$  slices at  $\alpha = 0$  (solid curves), 2 (dotted curves), 4 (dashed curves), and 8 (dot-dashed curves). The bottom two panels show  $L(\alpha)$  on six constant  $\Omega_0$  slices at  $\Omega_0 = 1$  (solid curves), 0.5 (dotted curves), 0.4 (short dashed curves), 0.3 (dot-dashed curves), 0.2 (dash-three-dotted curves), and 0.1 (long dashed curves).

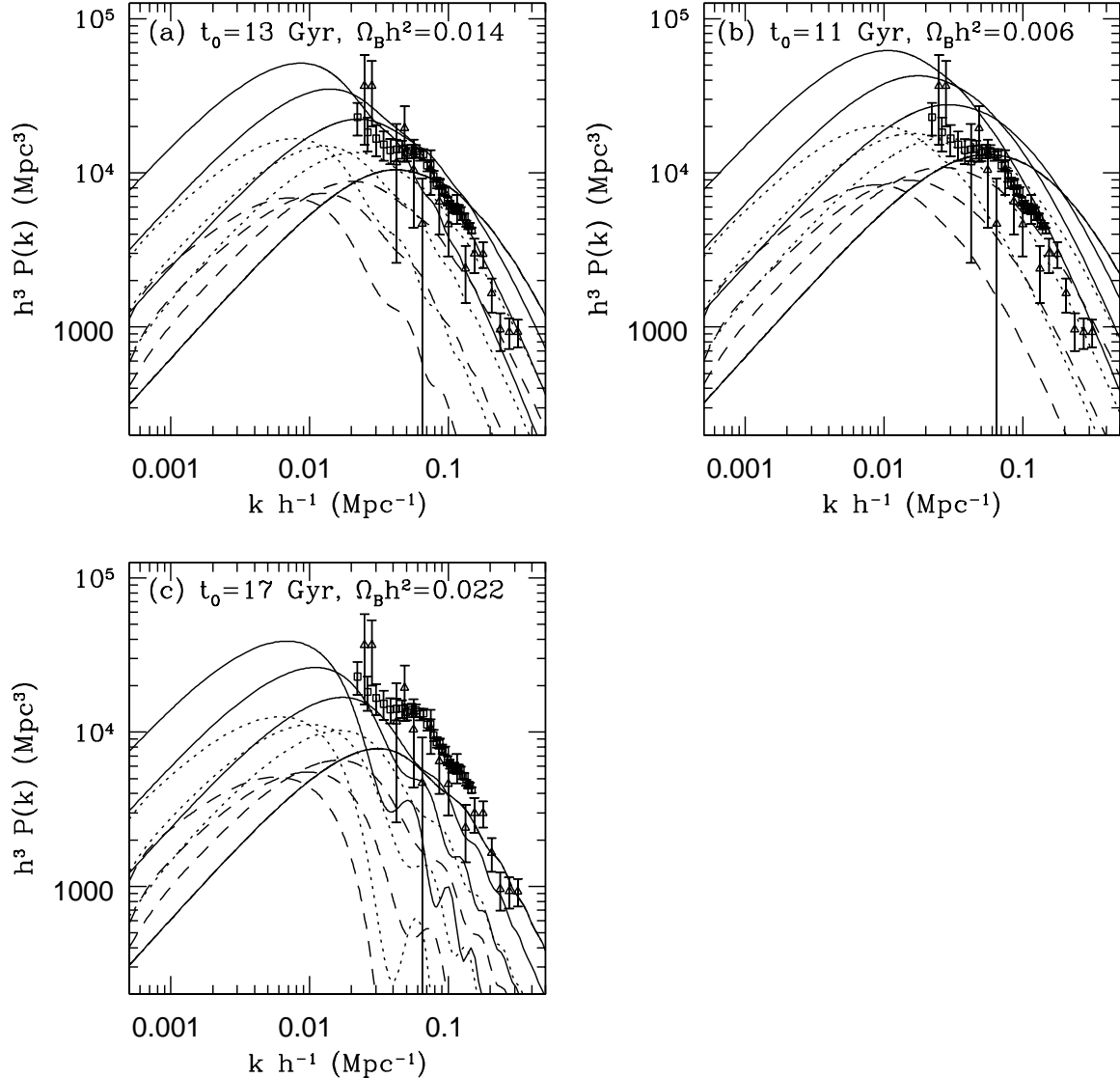


Fig. 10.— Fractional energy-density perturbation power spectra  $P(k)$  as a function of wavenumber  $k$ . These are normalized to the mean of the central  $Q_{\text{rms-PS}}$  values from the foreground-corrected quadrupole-included analysis and the foreground-uncorrected quadrupole-excluded analysis (for the corresponding values of the cosmological parameters). Panels *a*), *b*), and *c*) correspond to models with parameter values  $(t_0, \Omega_B h^2) = (13 \text{ Gyr}, 0.014)$ ,  $(11 \text{ Gyr}, 0.006)$ , and  $(17 \text{ Gyr}, 0.022)$ , respectively. Each panel shows 12 power spectra at three values of  $\alpha = 0$  (solid curves), 2 (dotted curves), and 4 (dashed curves) for four values of  $\Omega_0 = 1, 0.4, 0.2$ , and 0.1 in ascending order on the left axis of each panel. The triangles represent the linear real space power spectrum of the IRAS Point Source Catalogue Redshift Survey (PSCz) as estimated by Hamilton, Tegmark, & Padmanabhan (2000). Upper limits are not plotted. The squares represent the redshift-space galaxy power spectrum estimated from the 2dFGRS optical galaxy data (Percival et al. 2001).